Materials & Design 243 (2024) 113050

Contents lists available at ScienceDirect

Materials & Design

journal homepage: www.elsevier.com/locate/matdes

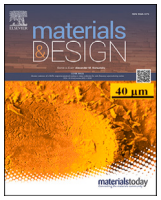

# Design method of immiscible dissimilar welding (Mg/Fe) based on CALPHAD and thermodynamic modelling

Chengwei Zang [a], Xiaoye Zhao [b], Hongbo Xia [b,c], Wei Wen [d], Zhuoming Tan [e], Caiwang Tan [b,*], Pedro E.J. Rivera-Díaz-del-Castillo [a,*]

[a] School of Engineering, University of Southampton, SO17 1BJ, United Kingdom
[b] State Key Laboratory of Advanced Welding and Joining, Harbin Institute of Technology, Harbin, 150001, China
[c] Zhengzhou Research Institute, Harbin Institute of Technology, Zhengzhou, 450018, China
[d] School of Engineering, Lancaster University, Lancaster LA1 4YW, United Kingdom
[e] School of Electromechanical and Automotive Engineering, Yantai University, Yantai, 264005, China

A B S T R A C T

Joining dissimilar metals is a major challenge in joining technology; the weldability of immiscible systems is especially challenging. In this study, a design methodology for dissimilar welding is suggested. The Miedema model and Toop model are developed to calculate the thermodynamics of quaternary alloy systems (Mg-Fe-Al-Cu). Finite element modelling (FEM) of temperature fields and the calculation of phase diagrams (CALPHAD) are combined to provide prerequisite information for modelling. As a test subject, laser welded lap configuration joints of AZ31B magnesium alloy and DP590 steel with a copper coating were put into the design scheme. The interfacial elemental diffusion and formation of intermetallics (IMCs) along the interface during the welding process are predicted. This simulation design scheme predicts the interfacial reaction kinetics and identifies whether the intermediate element works or not. The effects of the Cu coating thickness on the weld constitution, interfacial microstructures and mechanical properties were studied. Cu coating promotes the weld formation fostering the metallurgical reaction of the fusion zone (FZ) with the steel brazing interface. The mechanism of interfacial reactions during the welding-brazing process has been clarified. The Vickers hardness distribution across the interface shows that the Cu-IMCs are ductile.

## 1. Introduction

There is an increasing demand for multi-material components where dissimilar metal welding can enhance the product properties to meet the needs of the chemical, aerospace, and automotive industries [1,2]. However, dissimilar metals joining represents a challenge due to the difference in chemical and physical properties [3–5]. The problems in dissimilar welding can be divided into two categories: the immiscible systems, such as Fe/Mg [6–8] and Mg/Ti [9–11]; and the reactive systems, such as Fe/Al [12,13] and Ti/Al [14]. The former pairs are neither mutually soluble nor reactive. Metallurgical reactions are needed to achieve effective joints. In contrast, the latter pairs easily form coarse and brittle intermetallic compounds (IMCs), but this can be mitigated by controlling the processing parameters and using appropriate intermediate elements. The weldability of common engineering metal pairs is shown in Table 1 [15,16]. This is based on the similarity of atomic diameters and the electrochemical properties of each metal. This shows that only the Cu/Ni pair has excellent weldability, while the Mg/Fe and Mg/Ti pairs have the worst weldability, which indicates that the immiscible systems are the most difficult to join. Therefore, joint interfacial control is a top priority in addressing welding. The application of intermediate elements is proven to be an effective method to control the interfacial reactions [17].

The method for selecting the intermediate elements is crucially important. For immiscible systems, the intermediate elements should be highly soluble in both base metals. In this research, the Mg/Fe immiscible pair is chosen as object of study and validation of the model. Applying an intermediate element that is miscible in both Mg and Fe is an effective means of enhancing the interfacial reaction of joints, e.g. Sn [18], Zn [19,20,6], Ni [21,7,22,23,18,24] or Cu [25–27]. Al also plays an important role in connecting Mg/Fe. Liu et al. found that $Fe_2Al_5$ nanolayer in crystallographic terms matches well with both Mg and Fe [28]. The interplanar mismatches are less than 5% and interfaces are semicoherent, which reduces the interfacial energy and achieves a reliable connection. Elthalabawy et al. introduced a Cu interlayer during the eutectic bonding of AZ31 Mg alloy to 316L stainless steel [23,25]. Cu is reported to be beneficial by improving the wetting effect of the liquid eutectic phase on the steel surface. Liu et al. compared

* Corresponding authors.
*E-mail addresses:* tancaiwang@hitwh.edu.cn (C. Tan), p.rivera@soton.ac.uk (P.E.J. Rivera-Díaz-del-Castillo).

https://doi.org/10.1016/j.matdes.2024.113050
Received 10 January 2024; Received in revised form 24 May 2024; Accepted 27 May 2024
Available online 31 May 2024

**Table 1**
Weldability of common engineering metal pairs [15,16].

| Metal | Fe | Al | Ti | Ni | Mg | Cu |
|---|---|---|---|---|---|---|
| Fe | E | S | S | G | P | G |
| Al | S | E | S | S | S | S |
| Ti | S | S | E | S | P | S |
| Ni | G | S | S | E | S | E |
| Mg | S | S | S | S | E | S |
| Cu | S | S | S | E | S | E |

E-Excellent, G-Good, S-Satisfactory, P-Poor.

the effects of Ni and Cu interlayers on hybrid laser-tungsten inert gas (laser-TIG) welded joints [29,28]. The shear performance of Mg/steel joints with a Cu interlayer is reported to be superior to that of a Ni interlayer. They attribute the improved performance to the strengthening effect of $Mg_2Cu$ intermetallic. However, the above-mentioned reports only gave a preliminary description of the interfacial reaction products. The influence of the Cu interlayer thickness on mechanical properties and the formation mechanism of intermediate phases needs further research.

While experience plays a role in interlayer selection, there are also other approaches, such as computational thermodynamics and phase diagram analysis, that have been increasingly used in recent years. The researchers can usually apply the binary phase diagram to predict or analyse the interfacial reaction of dissimilar joints [30]. As the research progresses, the complexity of the elements involved in interfacial reactions increases. More theoretical work is needed to elucidate the mechanisms of dissimilar welding. Theoretical calculations of IMC formation can guide the selection of interlayers from a thermodynamic viewpoint. Some researchers built thermodynamic models to explain the elemental diffusion tendency and reaction mechanisms during the welding process. Tan et al. [31] calculated the formation enthalpy of the Mg-Ti-Al ternary system and the chemical potential of Al with different contents. Following this, they developed and applied Miedema-model-based thermodynamic calculations in laser welding-brazing of Mg/Fe [12] and Mg/Ti [32,9]. The formation enthalpy ($\Delta H$) and Gibbs free energy ($G_m$) of IMCs are calculated to explain the formation of prevailing phases. The lowest $G_m$ is an effective criterion for determining which reaction is most likely to occur first [12,7,33,34]. The elemental diffusion during the reaction is also analysed in detail based on the chemical potential ($\mu$). The elements usually diffuse from a region of high $\mu$ to one of low $\mu$ between the fusion zone (FZ) and substrates.

CALPHAD (CALculation of PHAse Diagrams) is a thermodynamic modelling and computational technique used in materials science and metallurgy to predict and understand the behaviour of alloys and other materials. CALPHAD can be used to model and predict phase equilibria and the microstructure evolution of dissimilar welds. Asadi et al. [35,36] applied the CALPHAD method to analyse the Fe-Ni-Ti, Fe–Ni–Cr, and Fe–Ti–Cr isothermal sections simultaneously in the Fe–Ni-Ti–Cr quaternary system, which aims to predict the formation of IMCs or possible phases in the weld zone of NiTi/austenitic stainless steel dissimilar laser joints. The Gibbs free energy of phases and chemical activity variations with temperature are combined to predict the phase formation during cooling. The calculated results of phase stability have a good agreement with the experiment results. Oliveira et al. [37,38] performed Scheil-Gulliver solidification through Thermo-Calc to explain the changes in microstructure that result from the thermal cycles during dissimilar welding of steel/CoCrFeMnNi high entropy alloy. Walker et al. [39] applied Ni and stainless steel as interlayers to Mg/steel using ultrasonic-interlayered resistance spot welding, which acquired a quite high joint efficiency. The thermodynamics and diffusion kinetics were calculated to reveal differences in nickel dissolution for the interlayers.

Based on the development of modelling and simulation in dissimilar welding, we aim to establish a design framework for the connection of dissimilar metals. In this work, the Miedema model was developed to calculate up to quaternary systems. Combined with the CALPHAD method and temperature field simulation, the progress of interfacial reaction during dissimilar welding can be predicted, which helps to improve the efficiency in selecting intermediate control elements, predict the elemental diffusion and reaction progress during welding, and therefore reduce the cost of experimental trials. In this work, the Mg/Fe miscible system with Cu interlayer was selected as the target object for validation. The influence of Cu coating thickness on laser welding-brazing Mg/steel joints was investigated. The joint appearance, mechanical properties, and interfacial microstructure were studied. Scheil solidification simulations were performed to analyse phase formation during cooling, combined with the analysis of temperature field simulation and thermodynamic calculations, the interfacial reaction mechanisms are clarified. The finite element modelling of temperature field is shown in the supplementary information section. The result shows the optimal Cu coating contributes to maximising the joint strength, here the optimal Cu coating thickness is defined as the thickness that leads to the highest joint strength and good interfacial microstructure.

## 2. Thermodynamic model

A thermodynamic model for the ternary systems needs to be derived based on the binary melt model. Geometric methods have been demonstrated to be a useful tool for calculating the thermodynamic properties of ternary systems based on information from binary systems. Previous research has indicated that these methods have produced results that are deemed acceptable [40–42]. Two approaches can be employed: symmetrical models or asymmetrical models [46]. It is preferable to use asymmetric models as they account for the effect of a third elemental species and reduce the deviation in calculations when compared with experimental data. Several asymmetric models have been proposed by Hillert [43], Toop [44], and Bonnier [45], while symmetrical models have been proposed by Kohler and Muggianu [46]. In this work, the Toop model is applied as an extension of the Miedema model. The building process of the geometric model is explained in the supporting information.

The excess free energy of the ternary alloy system can be expressed as:

$$\Delta G^E_{ABC} = \frac{x_B}{1-x_A}\Delta G^E_{AB}(x_A, 1-x_A) + \frac{x_C}{1-x_A}\Delta G^E_{AC}(x_A, 1-x_A) + (x_B+x_C)^2 \Delta G^E_{BC}\left(\frac{x_B}{x_B+x_C}, \frac{x_C}{x_B+x_C}\right) \quad (1)$$

where the excess free energy of any binary system can be calculated from Eq. 4 in the supplementary material section under Miedema Model.

The expression for the excess free energy in a quaternary alloy system becomes:

$$\begin{aligned}\Delta G^E_{ABCD} = {} & \frac{x_B}{1-x_A}\Delta G^E_{AB}(x_A, 1-x_A) + \frac{x_C}{1-x_A}\Delta G^E_{AC}(x_A, 1-x_A) \\ & + \frac{x_D}{1-x_A}\Delta G^E_{AD}(x_A, 1-x_A) \\ & + (x_B+x_C)^2 \Delta G^E_{BC}\left(\frac{x_B}{x_B+x_C}, \frac{x_C}{x_B+x_C}\right) \\ & + (x_B+x_D)^2 \Delta G^E_{BD}\left(\frac{x_B}{x_B+x_D}, \frac{x_D}{x_B+x_D}\right) \\ & + (x_C+x_D)^2 \Delta G^E_{CD}\left(\frac{x_C}{x_C+x_D}, \frac{x_D}{x_C+x_D}\right)\end{aligned} \quad (2)$$

From the definition of molar free energy, the molar free energy $G$ is equal to the sum of the ideal free energy $G^{ID}$ and the excess molar free energy $G^E$:

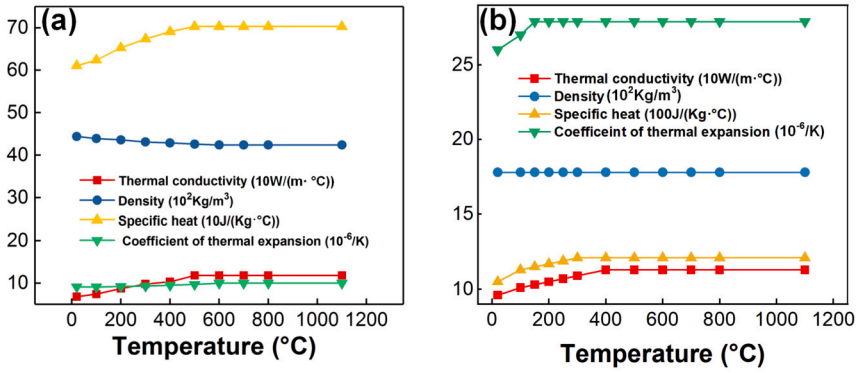


**Fig. 1.** Related parameters for temperature field simulation: (a) DP590; (b) AZ31B.

$$G = G^{ID} + G^{E} \tag{3}$$

According to the ideal solution model, the ideal free energy of ternary and quaternary alloys are:

$$G^{ID}_{ABC} = x_A G^*_A + x_B G^*_B + x_C G^*_C + RT[x_A \ln x_A + x_B \ln x_B + x_C \ln x_C] \tag{4}$$

$$G^{ID}_{ABCD} = x_A G^*_A + x_B G^*_B + x_C G^*_C + x_D G^*_D + RT[x_A \ln x_A + x_B \ln x_B + x_C \ln x_C + x_D \ln x_D] \tag{5}$$

where, $G^*_A, G^*_B, G^*_C, G^*_D$ are the molar free energies of the elements A, B, C and D respectively.

## 3. Temperature field simulation

In order to obtain the characteristics of the temperature field distribution at the joint interface for thermodynamic calculations, a three-dimensional instantaneous, nonlinear heat transfer temperature field for laser brazing of Mg/steel was established. Finite element simulation (FEM) of welding temperature field distribution was carried out by using MSC.MARC software [12,11]. The temperature cycle curves in different regions of the joint were obtained. The coating intermediate layer was ignored in the modelling due to its negligible thickness. The following assumptions were followed in the modelling:

(1) The ambient temperature was set at 20 °C, taking into account the convection and radiation heat transfer of the workpiece and the variation of the main thermophysical properties of the base metal with temperature change;

(2) The materials are isotropic. The dynamic wetting and spreading behaviour of the molten solder on the base metal was not considered;

(3) Only the thermal conduction between the workpiece and the atmosphere was considered, ignoring the heat transfer from the fixture to the workpiece.

Under such assumptions, the three-dimensional heat transfer steady state equation is obtained:

$$\rho C_P \frac{\partial T}{\partial t} = \frac{\partial}{\partial x}(k\frac{\partial T}{\partial x}) + \frac{\partial}{\partial y}(k\frac{\partial T}{\partial y}) + \frac{\partial}{\partial z}(k\frac{\partial T}{\partial z}) + q_a \tag{6}$$

where $C_P$ is the specific heat capacity of the metal, $k$ is the thermal conductivity and $q_a$ is the volumetric heat source within the action of the laser.

The initial temperature is chosen to be 20 °C and the boundary condition expression is:

$$k\frac{\partial T}{\partial z} = -q_{cr} \tag{7}$$

$$q_{cr} = \partial_{cr}(T - T_\infty) \tag{8}$$

where, $q_{cr}$ is the density of heat flow dissipated by convection and radiation, $\partial_{cr}$ is the coefficient of heat transfer, $T_\infty$ is the environmental temperature.

The energy of the laser decreases exponentially from the middle to both sides, following a Gaussian distribution of the heat source. Therefore, a Gaussian plane heat source was used in the simulation process and the linear energy was expressed as [47]:

$$q_s(x,y) = \frac{\alpha Q_s}{\pi r_s^2} \exp\left(-\frac{\alpha(x^2+y^2)}{r_s^2}\right) \tag{9}$$

where $\alpha = 0.15$ is the heat efficiency of the welding process, which is related to laser energy absorption by the AZ31B. $Q_s = 1300$ W and $r_s = 0.35$ mm are the effective power and the effective radius of the plane heat source.

A schematic diagram of mesh division is shown in supplementary material. The model was built in finite element simulation software MSC.MARC, using hexahedral elements with eight nodes. Laser welding-brazing takes the laser as a heat source and has the characteristics of fast heating and cooling speeds and large interfacial temperature gradients. Therefore, when dividing the mesh, mesh refinement was adopted in the laser irradiation region to improve the simulation accuracy, and coarse meshes were used in the base metal area far away from the weld to improve the calculation speed. Physical parameters such as thermal conductivity and the specific heat of the corresponding metals have different values at different temperatures. In order to make the model more accurate, the main thermophysical properties of the magnesium alloy [48] and the steel [47], and their variation with temperature, were added to MSC.MARC, as shown in Fig. 1.

The FEM-simulated result of the temperature distribution can provide basic data for thermodynamic analysis. As shown in Fig. 2 (a-b), the fusion line of the finite element model is compared with the actual fusion line of the welded joint cross section. To assess the precision of the developed model, a comparative analysis was performed between the simulated and experimental results, focusing on the temperature profiles at the testing point, as illustrated in Fig. 2 (c). The temperature measurement was carried out at a location 50 mm from the welding starting point and 2 mm from the seam. The comparison revealed a strong agreement between the experimental and numerical fusion lines, with the simulated thermal cycles closely matching the measured values. These findings provide strong validation of the model's reliability and predictive capability. There is always a variation of temperature gradient and microstructure at the interface of dissimilar laser welding-brazing joint [7,49,32]. For the purpose of analysis, it is usually divided into three parts: P1 intermediate region (close to Mg), P2 directly irradiated region (irradiated directly by laser) and P3 weld toe region (the seam tail). Fig. 3 shows the thermal cycle curves in the temperature field simulation for different areas at the joint interface. The peak temperature in the intermediate region, directly irradiated region and weld toe region are 963 °C, 1235 °C and 1153 °C, respectively. As the temperature curve of P3 (weld toe region) is quite similar to P2 (directly irradiated region), the following analysis will focus on P1 intermediate region and P2 directly irradiated region.

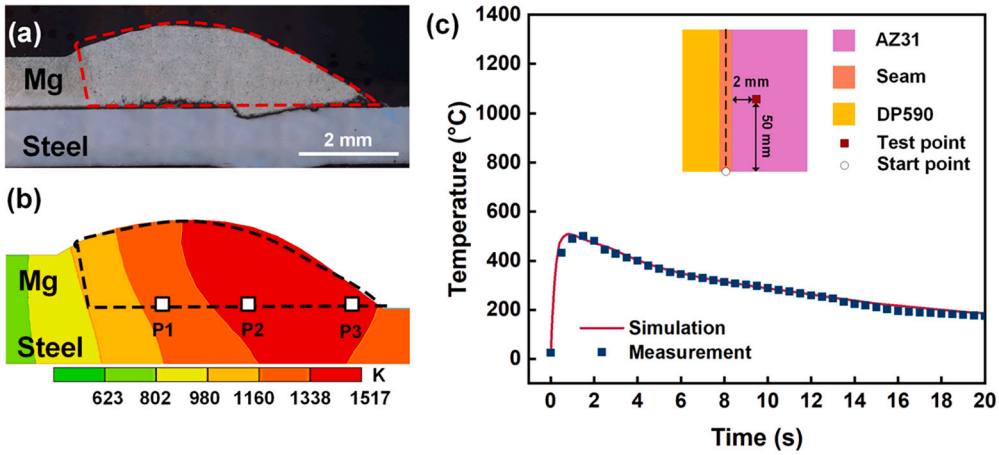


**Fig. 2.** Temperature field simulation of Mg/steel joint: (a-b) comparison diagram of fusion lines; (c) comparison between the simulated temperature and measured temperature.

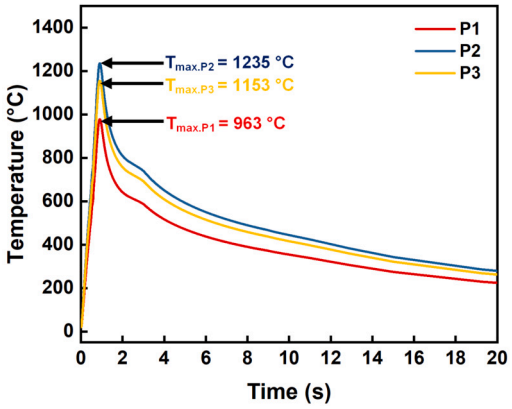


**Fig. 3.** Simulation results of thermal cycle curves in different regions at the joint interface.

## 4. Experimental procedures

### 4.1. Materials and electroplating process

The materials used in this work were 100 mm × 50 mm ×1 mm DP590 steel plates (Fe, ≤ 2.2 wt.% Mn, ≤ 0.8 wt.% Si, 0.18 wt.% C) and magnesium alloy AZ31B-H24 plates (Mg, 2.5-3.5 wt.% Al, 0.5-1.5 wt.% Zn, 0.2-0.5 wt.% Mn, 0.1 wt.% Si). AZ92D magnesium alloy filler (Mg, 8.3-9.3 wt.% Al, 1.7-2.3 wt.% Zn, 0.15-0.5 wt.% Mn, 0.05 wt.% Si) with 1.2 mm diameter was used.

The surface of the steel plate was ground with an angle grinder to remove the oxide film, and then cleaned by ultrasonic cleaning in acetone. Fig. 4 (a) is a schematic diagram of the electroplating process. Pure copper plate and steel plate are the anode and the cathode, respectively. The electroplating process was conducted in a 500 mL beaker containing the electroplating solution (55 g $K_4P_2O_7{\cdot}3H_2O$, 5 g $C_6H_{17}N_3O_7$, 12 g $CuSO_4{\cdot}5H_2O$, 6 g $Na_2HPO_4{\cdot}12H_2O$, 250 mL distilled water). Copper plating was carried out on the steel sheet with a DC power supply and a magnetic heating agitator. A cathodic current of 1 A/dm$^2$ was adopted at a temperature of 35 °C. The rotating speed of the magnetic agitator is 220 rpm. The thickness of Cu coating on the steel surface is controlled by setting the electroplating time for 30, 60, 90 and 120 min. The SEM morphology of the sections is shown in Fig. 4 (b-e). It can be seen that the coating thickness increased steadily with an increase in plating time, and the coating layer was uniform without obvious defects.

### 4.2. Laser welding-brazing process

The configuration of the laser welding-brazing process of magnesium/steel is shown in Fig. 5 (a). An overlapped Mg sheet on top was adopted. During the welding process, the laser beam irradiated the edge of the Mg sheet vertically. The filler wire was fed in front of the laser beam. Argon gas with 99.9% purity was blown at a 45° angle to the laser beam, and the gas flow was 10 L/min, which prevented the back surface of the seam and molten filler metal from oxidation. To reduce the burning loss of the upper Mg sheet, defocusing (positive defocusing 20 mm) welding mode was adopted. The main processing parameters employed in the research are listed in Table 2. Laser irradiation and stirring effects are the main factors that result in the variation of tem-

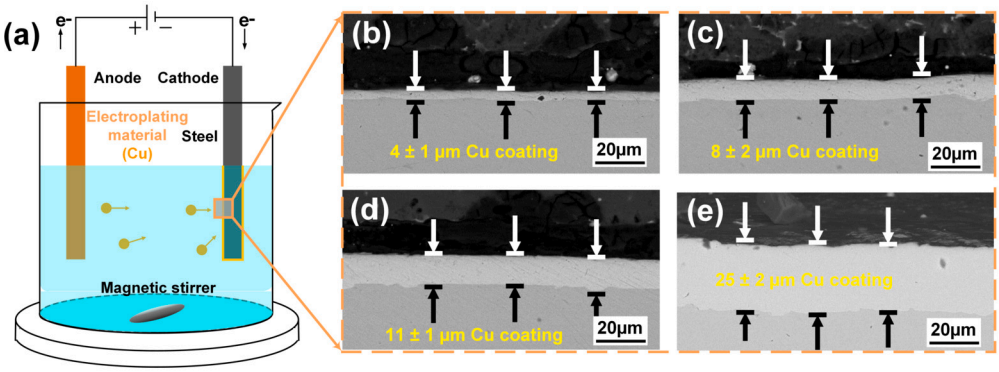


**Fig. 4.** (a) Schematic diagram of Cu electroplating on steel sheet; Cu coating thickness on steel surface with different electroplating times: (b) 0.5 h; (c) 1.0 h; (d) 1.5 h; (e) 2.0 h.

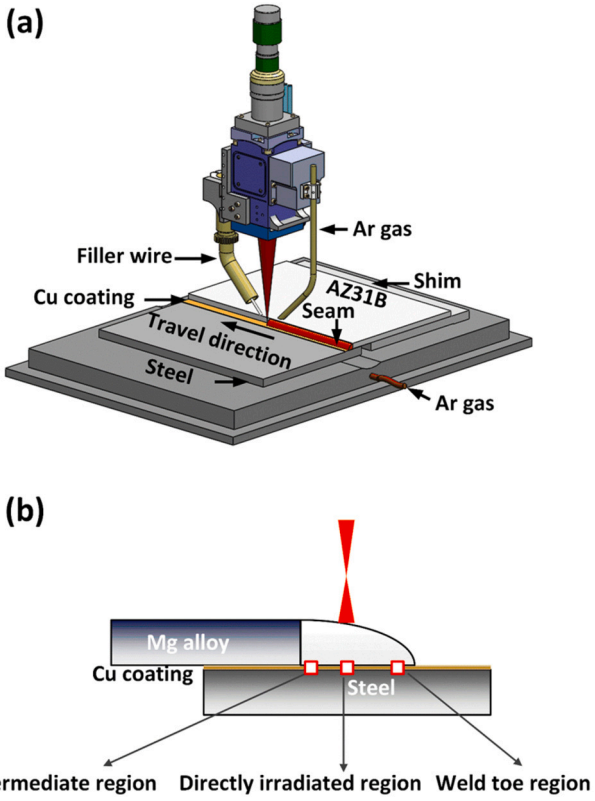


**Fig. 5.** (a) Schematic of the laser welding-brazing process to join AZ31B-Mg and Cu-coated DP590-steel; (b) diagram of Mg/steel cross-section and the deviation of different regions for analysis.

**Table 2**
Welding parameters used in laser welding-brazing.

| Welding parameters | Value |
|---|---|
| Laser power (W) | 1300 |
| Welding speed (m/min) | 0.25 |
| Defocus distance from the steel surface (mm) | +20 |
| Laser spot size (mm) | 0.35 |
| Flow rate of shielding gas Ar (L/min) | 10 |
| Wire feed speed (m/min) | 3 |

perature gradient and interfacial microstructure. The whole Mg/steel interfaces were divided into three regions for the purpose to analyse the joint conveniently: intermediate region (close to Mg), directly irradiated region (irradiated directly by laser) and weld toe region (the seam tail), as shown in Fig. 5 (b).

### 4.3. Analysis methods

After the LWB process, the cross-section samples of welded joints were wire cut and prepared through a standard metallographic process. DSX510 metallographic microscope (OLYMPUS, Japan) was used to observe the sample cross-section. The brazing interfacial microstructure was observed by field emission scanning electron microscope (FESEM) (Zeiss, Germany). The component of intermetallics and the distribution of interfacial elements were identified by energy dispersive spectrometry (EDS).

### 4.4. Mechanial testing

Specimens for tensile-shear experiments were cut into 90 mm × 10 mm units. To avoid bending the specimen during the tensile-shear process, shims were used on both sides of the specimen. The tensile-shear experiment was conducted by INSTRON 5967 universal material testing machine (Instron, USA) at a loading rate of 1 mm/min. Three tensile-shear specimens were selected from each lap joint group. The tensile-shear fracture load (N/mm) is the ratio of fracture load and specimen width.

## 5. Design methodology

### 5.1. Design methodology for dissimilar welding

The present approach focuses on an immiscible metal system for dissimilar welding in which the common denominator is the selection of intermediate elemental coatings to control interfacial reactions. IMCs formed from base metals can be coarse and brittle, and thermal straining upon contraction can appear as a result of cooling. The selection of intermediate elements (IEs) should satisfy the following criteria:

1. Moderate thermal conductivity and thermal expansion coefficient difference between IE and joint materials.
2. Lower formation enthalpy and Gibbs free energy of IE/substrate IMCs compared to base metal IMCs; this is to ensure the reactions occur first in the joint materials.
3. Newly formed IMCs should have lower brittleness and higher plasticity than original IMCs.

The detailed discussion of the methodology for reactive and immiscible systems is presented in the supporting information.

### 5.2. Binary formation enthalpy and ternary CALPHAD

Cu was selected as an intermediate element to improve the Mg/steel dissimilar bonding, due to its potential to promote metallurgical bonding between Mg and Fe. Cu has a good solubility with both Mg and Fe, which can facilitate interfacial reactions. Additionally, Cu has a lower melting point compared to Fe, which can enhance the wetting and spreading of the molten filler metal on the steel surface during the welding-brazing process. Fig. 6 (a) shows the formation enthalpy of different elemental pairs based on the Miedema model at 1226 °C. Mg-Fe can not react due to the positive standard molar enthalpy of formation, while Al-Fe phase is much easier to form at the surface of the steel. Although Cu-Fe has positive formation enthalpy, Cu can provide a board solid solution range with steel [50]. In addition, both Cu-Al and Mg-Cu pairs have negative formation enthalpy, which contributes to the interfacial reaction. The ternary isothermal sections were calculated for further prediction: Al-Fe-Mg, Al-Cu-Fe, Cu-Fe-Mg at 1000 °C based on TCFE10 database and Al-Cu-Mg at 600 °C based on TCMG5 database, as shown in Fig. 6 (b-e). For the Al-Fe-Mg isothermal section (Fig. 6 (b)), FeAl phase precipitates from liquid at the location with high Al concentration. FeAl is still the most common intermetallic in the Al-Cu-Fe system, as shown in Fig. 6 (c). It indicates that the FeAl phase will form at the steel surface if the temperature reaches a high temperature (1000 °C). In the region of high Fe concentration, Fe and Cu do not react to each other and are separated as BCC+FCC. It assumed that Cu would dissolve into a steel substrate. There is no obvious metallurgical reaction in the Cu-Fe-Mg system (Fig. 6 (d)). The Al-Cu-Mg reaction should occur at the seam. Therefore, the analysis in Fig. 6 (e) should be located on high Mg concentration. C15_LAVES phase ($Mg_2$(Cu, Al)) would generate from the liquid.

### 5.3. Quaternary modelling at FZ/steel interface

In the calculation of Gibbs free energy and chemical potential of the Mg-Cu-Al-Fe quaternary elements system, the influence of the trace elements Zn, Mn, and Si in the Mg-based filler wire was neglected. At the beginning of welding (Stage 1), the interface of the joint was assumed to be an AZ92-Cu-Fe system, and the content of Al was fixed. The value

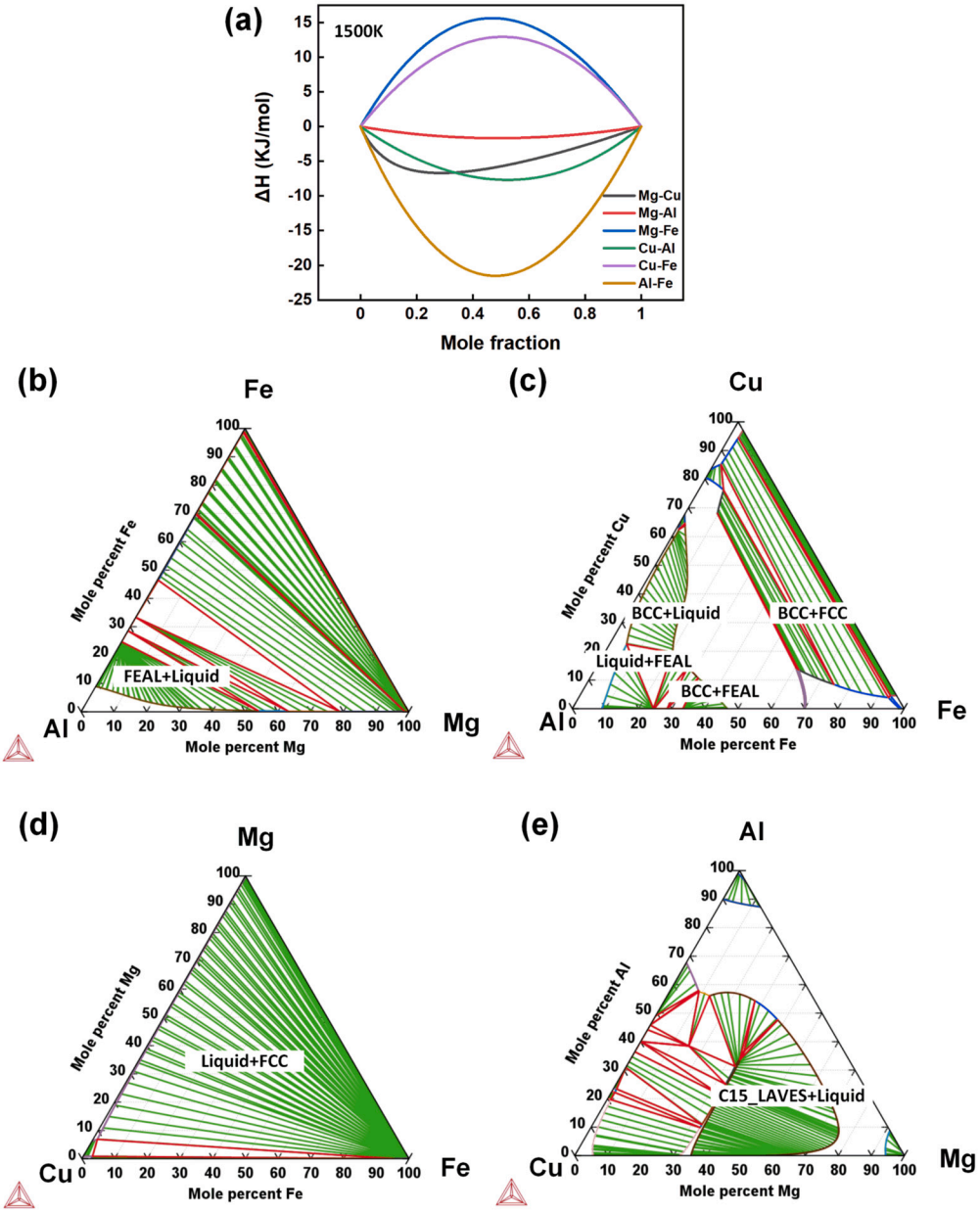


**Fig. 6.** (a) Formation enthalpy of binary elemental system; (b-e) CALPHAD ternary isothermal section of Al-Fe-Mg, Al-Cu-Fe, Cu-Fe-Mg at 1000 °C and Al-Cu-Mg at 600 °C, respectively.

is referred to the content of Al in AZ92 welding wire (9 wt%). The diffusion trend of Cu and Al atoms is analysed first. Then the subsequent reactions are analysed based on the diffusion of Cu/Al elements (Stage 2). Cu content at the weld/steel interface in the directly irradiated region was set to 10.1 at.%, and Fe content in the fusion zone far away from the interface was set to 4.7 at.%.

Fig. 7 shows the thermodynamic calculation results of the directly irradiated region, which aim to clarify the formation mechanism of the FeAl phase. In Stage 1, the content of Al in the AZ92-Cu-Fe system was set to 0.101, as shown in Fig. 7 (a-b). The analysis range of Fig. 7 (a) was limited to 20 at.% of Cu content, as shown in the black virtual box. The chemical potential of Cu at different specific Cu contents (0.001/0.051/0.101/0.151) was analysed, as shown by the red dotted lines. The lowest value of chemical potential on each red dotted line is highlighted by a black square. It can be seen that Cu tends to aggregate at a certain distance from the steel substrate surface. As shown in Fig. 7 (b), it becomes clear that Al atoms diffuse from Cu and Mg to Fe. Al atoms tend to diffuse and aggregate to the steel substrate in the Mg-Cu-Al-Fe quaternary system.

In stage 2, under the action of direct laser shock and flow field agitation, Cu flowed to both sides of the seam and the content of Cu in the directly irradiated region should be very low. According to the analysis in Stage 1, Cu does not gather on the steel substrate surface. Therefore, the content of Cu on the steel substrate surface was set to 0.101 to facilitate the analysis of the chemical potential and Gibbs free energy between Mg-Al-Fe and the steel. As shown in Fig. 7 (c), Al diffuses easily to the Fe side in this system. The Mg content at the steel surface is very low, limiting its content to less than 0.051, as shown by the black dotted line in the figure. Besides, the diffusion trend of Al under this condition is shown by the small red arrow. It is found that Al still diffuses to the steel substrate when the Al content is low. Fig. 7 (d) shows the Gibbs free energy of the (Mg-Al-Fe)-0.101Cu system, which indicates the formation of FeAl phase.

Fig. 8 shows the calculation results for the chemical potential at different stages in the intermediate region, focusing on the diffusion

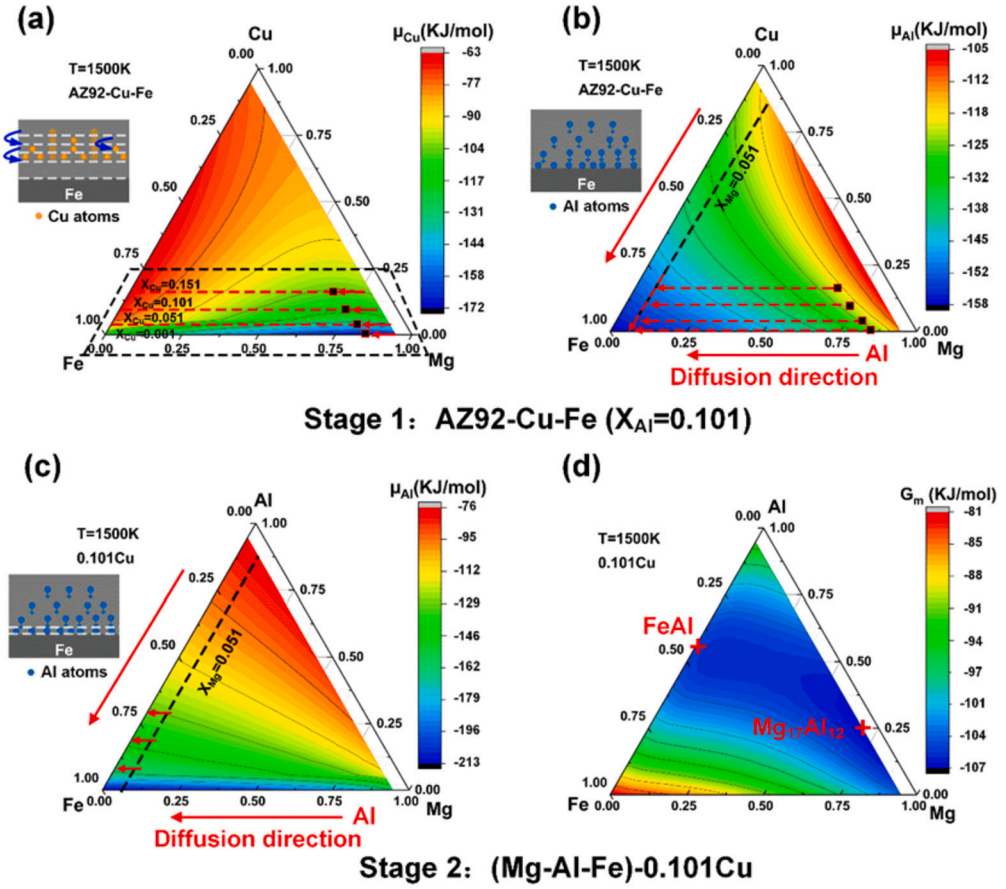


**Fig. 7.** Thermodynamic calculation of the directly irradiated region at laser welding-brazing interface of magnesium/copper-plated steel: (a-b) chemical potential of Cu and Al in AZ92-Cu-Fe system; (c) the chemical potential of Al at the steel interface; (d) Gibbs free energy at the steel interface.

of Cu and Al at the Mg/steel interface and the formation kinetics of reaction products.

Different from the directly irradiated region, laser shock and stirring effects in the transition area are weaker and Cu in the irradiated region would diffuse to the area under the action of stirring. In stage 1, Cu initially diffuses from the interface and its content was set as 0.25-0.3. Similar to the analysis of the irradiated region, Cu tends to diffuse towards Mg (seam) and aggregates at a certain distance from the surface of the steel substrate. Similarly, the diffusion of Al element in this region is the same as that in the directly irradiated region, which mainly diffuses towards the steel.

In the seam far from the steel substrate, the content of Fe was set to 0.097. The (Mg-Al-Cu)-0.097Fe system was established to analyse the diffusion of Cu and Al in this area, as shown in Fig. 8 (c-d). Cu atoms still tend to diffuse to the place with high Mg content. Al atoms are easy to combine with Mg atoms by phase diffusion, which explains the formation of an ordinary phase ($Mg_{17}Al_{12}$) in the AZ92 fusion zone.

Fig. 9 shows Gibbs free energy calculation results at the weld interface in the intermediate region. The Mg-Al-Cu Laves phase is generated at the interface, and its content is supposed to be Al 40-50 at.%, Cu 40-50 at.%, Mg 20-25 at.%. The Mg content in the AZ92 seam is relatively high. So the lower limitation of Mg is set to be quite high, as the black dotted line in Fig. 9 (b).

## 6. Results and discussion

### 6.1. Joint appearances and cross-sections

Fig. 10 shows the Mg/steel laser welding-brazing appearance and joint cross-section with different Cu coating thicknesses. As shown in Fig. 10 (a), the appearance of Mg/steel with 4 μm coating was serrated and contractile at the end of the seam, while the appearance of Mg/steel with Cu coating was relatively smooth and showed no significant defects. By comparing the various cross-section morphologies, it can be seen that the wire filler deposition was stable. The surface of the steel edge was kept flat generally. Only a small fraction of the area irradiated directly by the laser melted slightly, which indicated that the laser energy was reduced by the laser processing parameters of positive defocusing and low power, and the purpose of welding-brazing was attained.

### 6.2. Interfacial mircostructure

Fig. 11 presents the interfacial microstructure of laser welded-brazed Mg/steel with different Cu coating thicknesses. The microstructure in the intermediate region and the weld toe region were quite similar, while the morphology in the directly irradiated region was different to the other regions. This is attributed to the difference in Cu content in different regions. The authors consider that the lack of Cu in the directly irradiated region is mostly attributed to the flow field caused by laser shock. Some researchers simulated the flow field distribution in laser welding-brazing joints [51]. The negative surface tension gradient drove the molten metal to flow from the centre of the welding pool to the edges on both sides, which initially had a trend of annular flow. The Cu coating melted completely in the directly irradiated region and therefore moved away to the edges. To identify the precipitated phase compositions along the interface, EDS points (Table 3) and line scans were conducted to quantify the elemental distribution along the fusion zone/steel interface in the directly irradiated region. The corresponding positions are highlighted in Fig. 11, and the scan results are shown in Fig. 12.

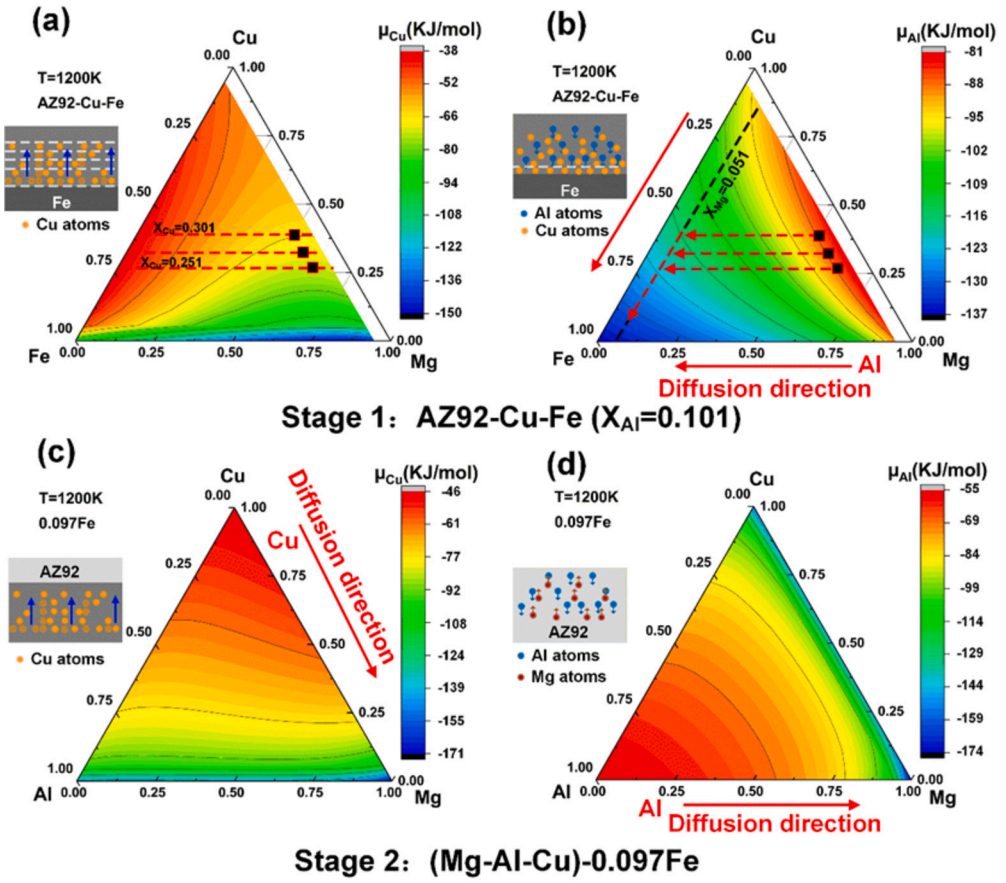


**Fig. 8.** Thermodynamic calculation of the intermediate region of laser welding-brazing joint of magnesium/copper-plated steel: (a-b) chemical potential of Cu and Al in AZ92-Cu-Fe system; (c-d) chemical potential of Cu and Al in AZ92 molten pool.

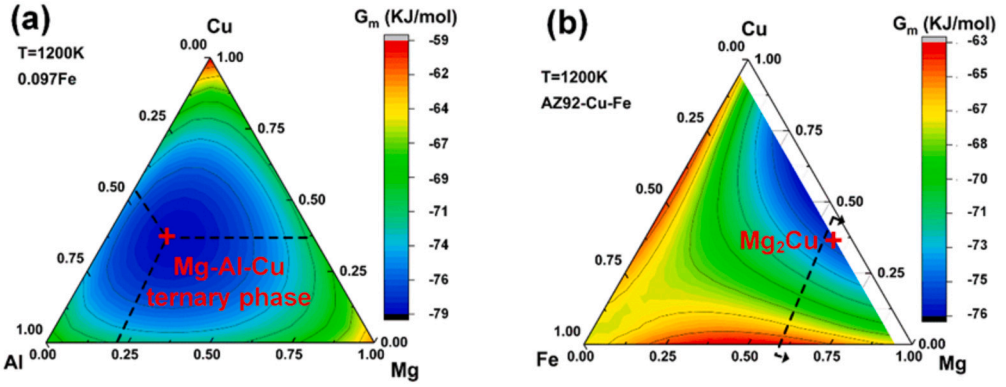


**Fig. 9.** Thermodynamic calculation of the intermediate region of laser welding-brazing joint of magnesium/copper-plated steel: (a) Gibbs free energy of (Mg-Al-Cu)-0.097Fe quaternary system; (b) Gibbs free energy of AZ92-Cu-Fe system.

**4 μm**

Fig. 11 (a-c) shows the SEM morphology of the laser welded-brazed Mg/steel joint with a Cu coating thicknesses of 4 μm. The surface of steel melted slightly in the directly irradiated region while the surface was relatively flat in the other regions. There was no adequate metallurgical reaction along the fusion zone (FZ)/steel interface. In the intermediate region, $Mg_{17}Al_{12}$ (P1) precipitates distributed on the α-Mg matrix near the interface were observed. A thin and homogeneous reaction layer was observed in the directly irradiated region and the corresponding line scanning analysis results are shown in Fig. 12 (a). Al atoms were aggregated at the marked reaction layer, which indicates that Al atoms diffused from AZ92 filler to the FZ/steel interface and FeAl phase could be identified. The reaction layer played an important role in the metallurgical bonding of Mg/steel. In the weld toe region, there was full of a coral-shaped structure near the interface. A higher magnification image is shown in the inset in Fig. 11 (c) which shows a lamellar eutectic structure. EDS analysis of P2 point is composed of 73.95 at.% Mg, 1.86 at.% Al, 2.11 at.% Fe, 22.08 at.% Cu. Combined with the Mg-Cu phase diagram, $Mg_2Cu$ is generated at the interface. P2 is identified as the eutectic structure of Mg-Cu (α-Mg+$Mg_2Cu$). The presence of the eutectic structure was caused by a eutectic reaction in the liquid at 487 ºC [24]: $L \xrightarrow{487\,^{\circ}C} \alpha\text{-Mg} + Mg_2Cu$.

**8 μm**

The interfacial microstructure changed greatly when increasing the Cu coating thickness to 8 μm, as shown in Fig. 11 (d-f). A large number of intermetallic compounds are formed in the intermediate region. The

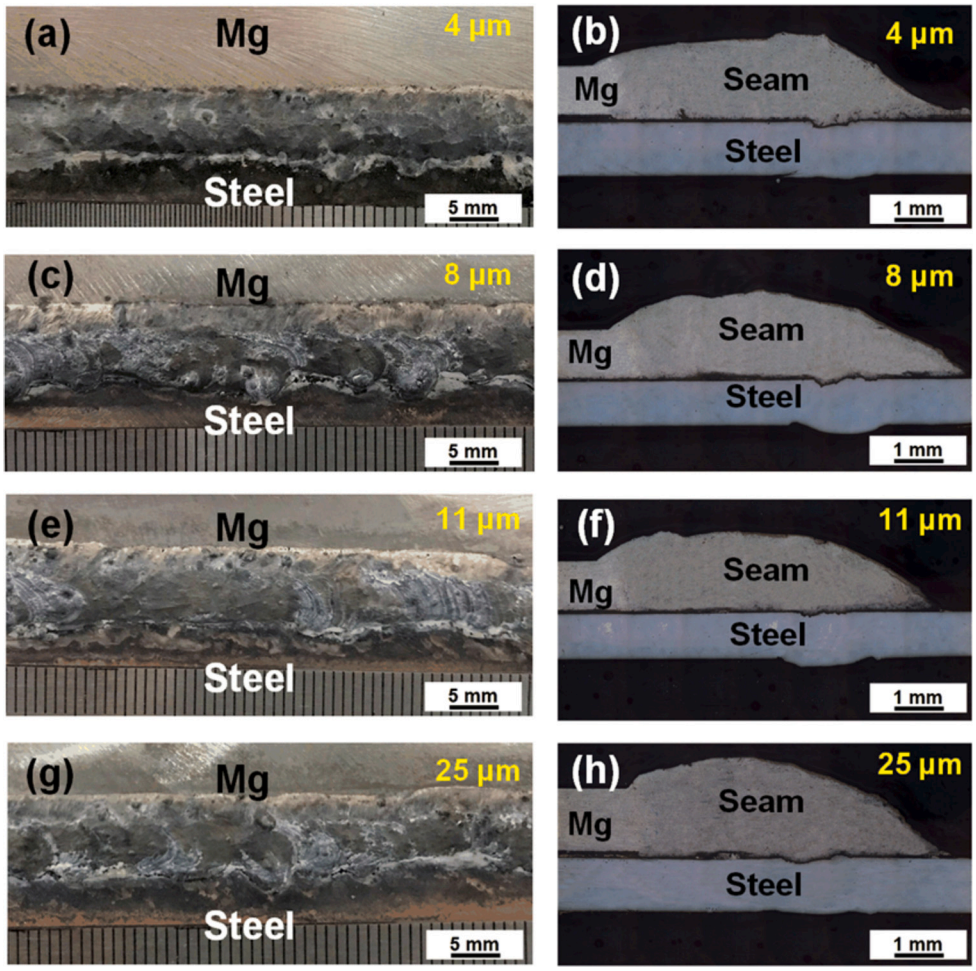


**Fig. 10.** Mg-Steel laser welding-brazing appearance and joint cross-section morphology with different Cu coating thickness.

**Table 3**
EDS analysis of element content and possible phases of the points shown in Fig. 11 (at. %).

| Point | Mg | Al | Fe | Cu | Possible phase |
|---|---|---|---|---|---|
| P1 | 59.30 | 26.89 | 13.59 | 0.22 | $Mg_{17}Al_{12}$ |
| P2 | 73.95 | 1.86 | 2.11 | 22.08 | ($\alpha$-Mg+$Mg_2Cu$) |
| P3 | 74.72 | 0.01 | 0.76 | 24.51 | ($\alpha$-Mg+$Mg_2Cu$) |
| P4 | 37.28 | 14.64 | 1.52 | 46.56 | Laves Phase |
| P5 | 37.69 | 20.34 | 0.33 | 41.64 | Laves Phase |
| P6 | 67.34 | 0.30 | 0.37 | 32.00 | $Mg_2Cu$ |
| P7 | 32.14 | 20.62 | 5.97 | 41.27 | Laves Phase |
| P8 | 80.45 | 0.24 | 0.97 | 18.34 | ($\alpha$-Mg+$Mg_2Cu$) |
| P9 | 93.65 | 0.79 | 0.48 | 5.08 | $\alpha$-Mg |
| P10 | 67.75 | 2.24 | 0.49 | 29.52 | $Mg_2Cu$ |
| P11 | 36.14 | 17.35 | 0.90 | 45.61 | Laves Phase |
| P12 | 65.34 | 0.25 | 0.95 | 33.46 | $Mg_2Cu$ |
| P13 | 40.83 | 11.17 | 1.15 | 46.85 | Laves Phase |
| P14 | 68.01 | 0.22 | 0.72 | 31.05 | $Mg_2Cu$ |

composition of the grey matrix P3 near the interface is similar to P2, which can be identified as a ($\alpha$-Mg+$Mg_2Cu$) eutectic structure. There were some particles (P4) distributed densely across the matrix displaying an $\alpha$-Mg+$Mg_2Cu$ eutectic structure. The EDS analysis in Table 3 shows that P4 is composed of 37.28 at.% Mg, 14.46 at.% Al, 1.52 at.% Fe, 46.56 at.% Cu, which was identified as C15 Laves phase Mg(Cu, Al)$_2$. A similar reaction product was reported in a previous study of laser-welded Mg/Cu joints [37]. The formation of the Mg(Cu, Al)$_2$ phase was attributed to some Al atoms replacing part of Cu atoms in the $MgCu_2$ Laves phase. It was estimated as semi-stoichiometric phases in agreement with the formula Mg $(Al_xCu_{1-x})_2$ Laves. In addition, the Laves phase and ($\alpha$-Mg+$Mg_2Cu$) eutectic structure were produced at almost the same temperature. Therefore, the Laves phase was distributed within the eutectic structure as discrete blocks after solidification. It should be noticed that a visible long crack was found on the eutectic microstructure in this region, which is thought to be caused by the residual stress resulting from the solidification of the molten pool and thick brittle intermetallic compound layer. The crack reduces the mechanical properties of the joint. In the weld toe region, the volume of the intermetallic compounds increased significantly and the reaction became more pronounced. There were large Laves phases (P5) and $Mg_2Cu$ phases (P6: 67.34 at.% Mg, 32.00 at.% Cu) distributed in FZ, which was quite different to that in the 4 μm weld toe region.

**11 μm**

When the Cu coating thickness reached 11 μm, the brazing interfacial reaction of the Mg/steel joint was similar to that of 8 μm Cu coating thickness. The number of intermetallic compounds did not change significantly. The diffusion of elements in the directly irradiated region was similar, which can be verified by the width of the diffusion zone in Fig. 12 (b-c).

**25 μm**

For the 25 μm Cu coating thickness, a new island-like structure developed along the interface within the matrix of the Mg-Cu eutectic. The corresponding EDS result of P12 indicated that this phase was composed of 65.34 at.% Mg, 0.25 at.% Al, 0.95 at.% Fe and 33.46 at.% Cu, suggesting the precipitation of $Mg_2Cu$ IMCs based on the Mg-Cu binary phase diagram. The increase in Cu resulted in the transformation of ($\alpha$-Mg+$Mg_2Cu$) eutectic structure to the $Mg_2Cu$ phase (P12, P14). Large

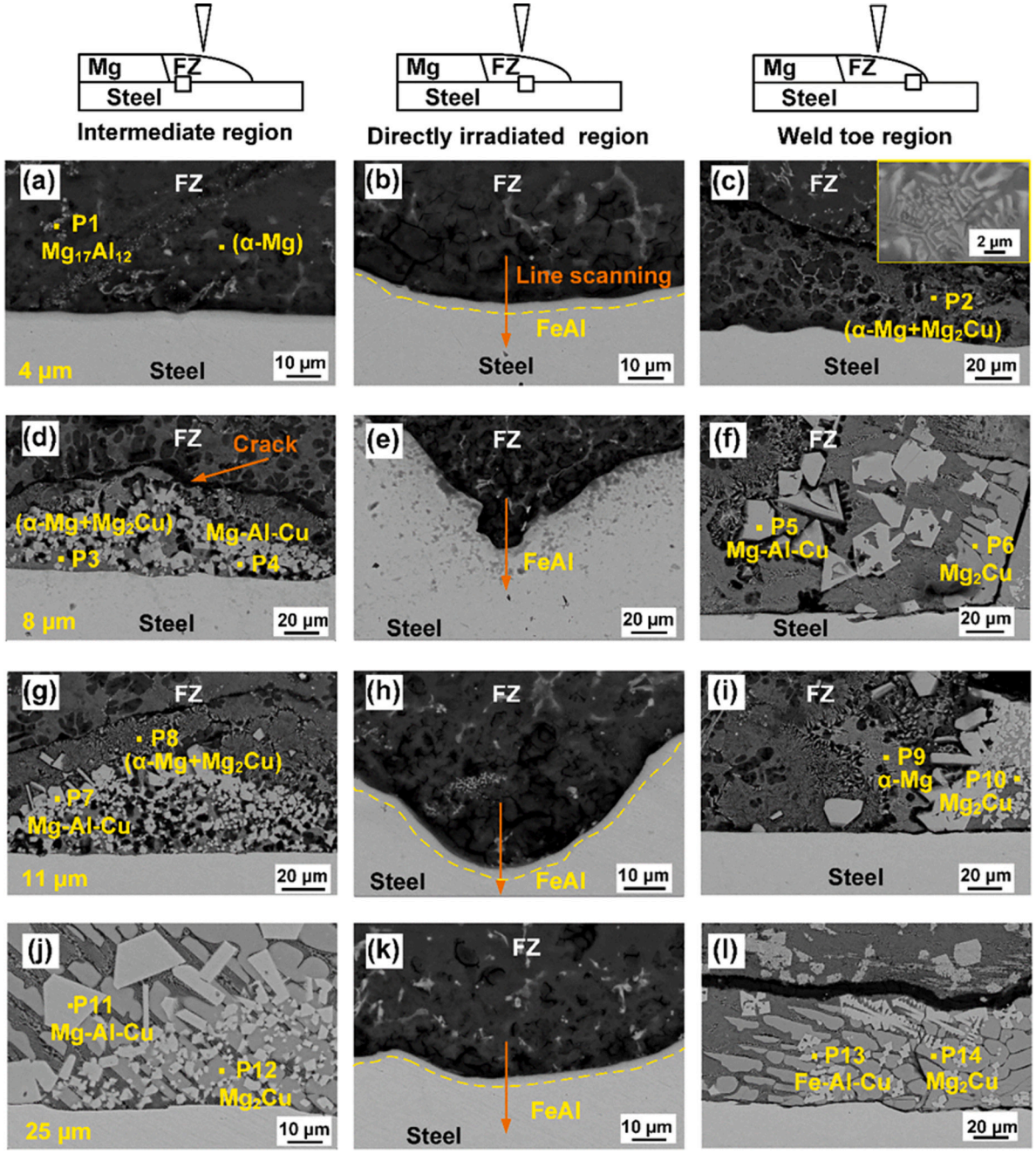


**Fig. 11.** SEM morphology of laser welded-brazed Mg/steel joints with different Cu coating thicknesses: (a)-(c) 4 μm; (d)-(f) 8 μm; (g)-(i) 11 μm; (j)-(l) 25 μm.

Mg-Al-Cu Laves structures were distributed into $Mg_2Cu$ in the intermediate region and weld toe region. The size of partial Laves phases (P11) increased significantly as shown in Fig. 11 (j). Besides, a long strip crack was generated in the weld toe region which was similar to that in the 8 μm-coating-thickness joint as described above. Such cracks are related to the growth of brittle intermetallic compounds caused by the increase in coating thickness.

Fig. 12 shows the EDS line scan results across the interface regions shown in Fig. 11. A visible Al elemental aggregation can be observed at the diffusion zone. The reaction layer can be determined to be FeAl due to its stoichiometry. The width of Al aggregation agrees with the thickness of the reaction layer shown in Fig. 11, which is about 5 μm. It should be noted that the width of the diffusion zone increased gradually with the increase in Cu coating thickness, which indicates that Cu promotes Mg/steel joint interdiffusion, enhancing bonding. It is beneficial to realize interfacial metallurgical bonding of the Mg/steel joint. In addition, the presence of Cu in the directly irradiated region is hardly observed when the coating thickness is low, as shown in Fig. 12 (a-b). Cu migrates to other regions of FZ under the action of laser impact and flow field agitation. Therefore, Cu does not play a role in the metallurgical reactions in the directly irradiated region. When the Cu coating thickness reaches a certain thickness, as shown in Fig. 12 (c-d), some residual Cu along the interface reacts with Mg producing $Mg_2Cu$, following a 60/30 atom ratio. Fluctuations of Cu amounts at the interfacial diffusion zone are attributed to the linear scanning analysis line passed the position containing $Mg_2Cu$ compounds, as shown in Fig. 11 (h, k). In fact, the content of Cu is still very low for the whole directly irradiated region, as shown by the line scans.

Fig. 13 shows EDS map scanning analysis of the elemental distribution across the directly irradiated region interface with 11 μm Cu coating. High-contrast maps indicate the enrichment of the corresponding element in the region. It becomes clear that the segregation of Al

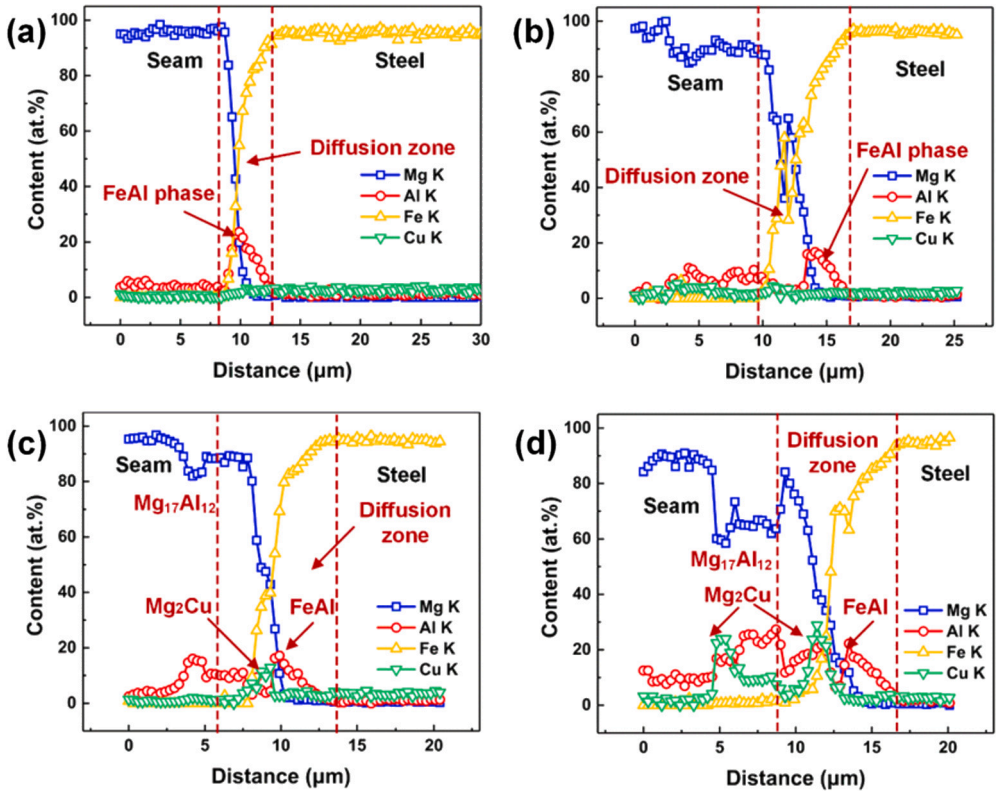


**Fig. 12.** EDS line scanning results across directly irradiated region interface with different Cu coating thicknesses shown in Fig. 11: (a) 4 μm; (b) 8 μm; (c) 11 μm; (d) 25 μm.

exists close to or at the interface, which implies there is a diffusion of Al from FZ to steel. The Al segregation layer along the steel surface perfectly matches the reaction layer in the SEM image, which proves the presence of a stable FeAl reaction layer. The thickness of FeAl reaction layer is the same as the thickness of the Al segregation layer. Additionally, extra Al is concentrated in the FZ and dispersed in the precipitated Mg-Al phases, some of them show a trace of Cu. This indicates that Cu atoms can dissolve into the Mg-Al phase and form the Mg-Al-Cu LAVES phase. As mentioned earlier, the content of Cu elements in the directly irradiated region is very low. Most of the Cu was displaced into adjacent regions under the impact force and flow field of the laser. Only a reduced amount of Cu reacts to form the Mg-Cu eutectic structure and the Mg-Al-Cu ternary phase in the fusion zone. In addition, it can be seen there is a red high contrast in the lower part of Fig. 13 (e). This indicates that Cu atoms have been highly dissolved into the steel substrate. Following the thermodynamic simulation section this contributes to attracting Al atoms to the steel.

### 6.3. Mechanical properties

The Vickers microhardness distribution across the joints with different Cu coating thicknesses is shown in Fig. 14. The hardness uniformly increases from the AZ92D seam to the steel substrate for all different coatings. At the interface of the Mg/steel, the microhardness is significantly increased. However, the interfacial hardness varies with different Cu coatings, which decreases from 120 HV (4 μm, 8 μm Cu coating thickness) to 80 HV (25 μm Cu coating thickness). The average value of interfacial hardness is lower than that of Ni coating (about 140 HV) as discussed in [7]. The low interfacial hardness indicates that the IMCs generated in Mg/steel joints with Cu coating are more ductile, which is beneficial to mechanical properties. In addition, it is interesting that the hardness of steel substrates decreases with increasing Cu coating thickness. This may be attributed to the diffusion of Cu to steel as Cu is softer than Fe.

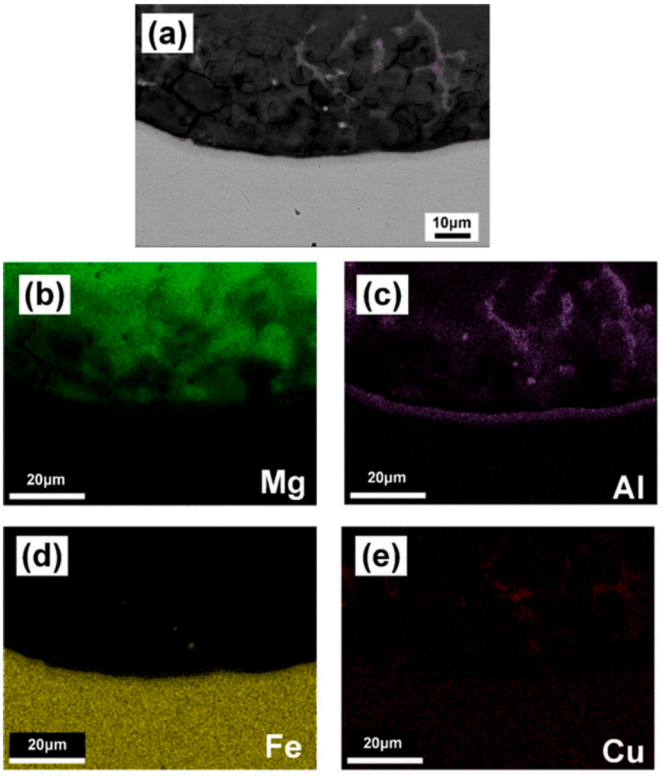


**Fig. 13.** The EDS map scanning results across directly irradiated region interface with 11 μm Cu coating: (a) SEM morphology; (b-e) elemental distribution of Mg, Al, Fe, and Cu, respectively.

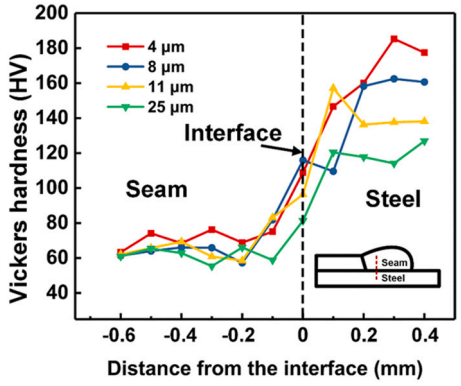


**Fig. 14.** The variation of hardness distribution across the joints in the intermediate region with different Cu coating thickness.

Tensile tests were carried out on Mg/steel laser welding-brazing joints with different Cu coating thicknesses. The results are shown in Fig. 15 (a). For the Mg/steel laser welding-brazing joint with 4 μm Cu coating thickness, the joint performance is the lowest and the cracks propagated from the interface. Combined with the interfacial microstructure, it is easy to find that there is a large number of $\alpha$-Mg+$Mg_2Cu$ eutectic structures with a network distribution in the weld toe region, which would become the origin of cracks and cause an interfacial fracture. With the increase in coating thickness, the overall tear-shear fracture load first increases to reach a maximum of 271 N/mm, almost equivalent to the shear fracture strength of the AZ31B alloy. In the laser-welded lap joints between magnesium and steel, our joint strength is the highest compared to all previously reported literature, as shown in Fig. 15 (b) and Table 4. This indicated that the addition of Cu can significantly control the metallurgical reaction at the interface of Mg/steel joints, thus solving the problem of weak Mg/steel joints.

According to Laukant et al. [52], FeAl phase with a thickness lower than 10 μm is beneficial to improve the mechanical properties of the joint. The previous SEM and EDS analysis of the directly irradiated region at the joint interface shows a 5 μm thick FeAl reaction layer. The metallurgical reaction between Fe/Al is an important guarantee to improve the bonding strength of Mg/steel, which was verified by our previous study [7]. In addition, the more ductile Cu-IMCs also contribute to the mechanical properties.

For Mg/steel laser welding-brazing joints with different coating thicknesses, they can be divided into two types according to different fracture paths: interfacial fracture and seam fracture. Fig. 16 shows the fracture path and fracture morphology of the Mg/steel laser welding-brazing joint with a Cu coating thickness of 4 μm. The EDS analysis of the selected points is shown in Table 5. Under this condition, the joint was fractured along the brazing interface. As can be seen from the fracture cross-section (Fig. 17 (b, c)), the clear FeAl reaction layer (P2: Al 46.11 at.%, Fe 50.50 at.%) (P3: Al 32.27 at.%, Fe 32.27 at.%) can be found at the welding seam and steel edge along the fracture path. Except for lump-like $Mg_{17}Al_{12}$, residual $\alpha$-Mg+FeAl particles (P4:

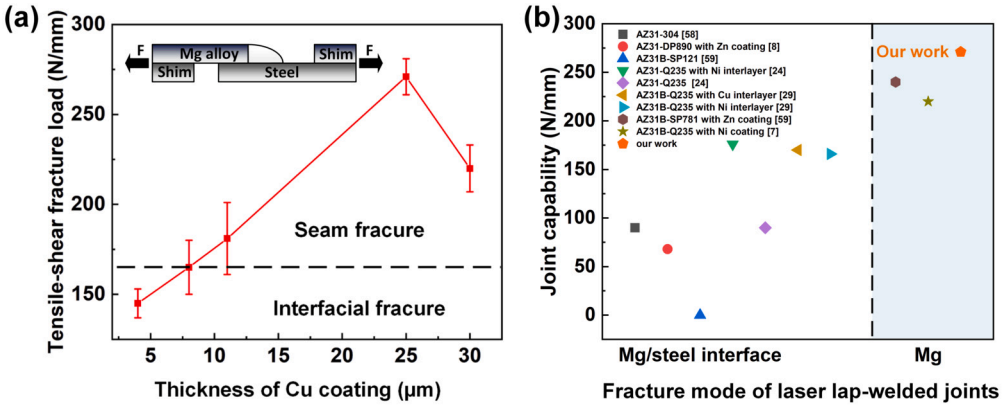


**Fig. 15.** (a) Fracture load of magnesium/steel joint with different Cu coating thickness; (b) Joint capability of laser lap-welded joints from literature.

**Table 4**
Joint strength and fracture location of lap-welded Mg/steel joints shown in Fig. 15, data comes from Ref. [53].

| Base metals | | Interlayer or coating | Welding methods | Joint strength | Fracture mode | Refs. |
|---|---|---|---|---|---|---|
| Mg alloys (thickness) | Steel (thickness) | Material (thickness) | | | | |
| AZ31 (1.7 mm) | 304 steel (1.2 mm) | None | Laser-TIG | Tensile strength of 90 MPa | Interfacial fracture | [54] |
| AZ31 (1.5 mm) | DP890 (1.5 mm) | Zn coating (10-15 μm) | Laser-TIG | Shear strength of 68 MPa | Interfacial fracture | [8] |
| AZ31B (3 mm) | SP121 (1.2 mm) | None | Laser | 0 | - | [55] |
| AZ31B (3 mm) | SP781 (1.2 mm) | Zn coating (9 μm) | Laser | 6000 N with 25 mm width sample | Fusion zone | [55] |
| AZ31 (1.7 mm) | Q235 (1.2 mm) | Ni (100 μm) | Laser-TIG | Shear strength of 176 MPa (1 mm welding) | Interfacial fracture | [24] |
| AZ31 (1.7 mm) | Q235 (1.2 mm) | None | Laser-TIG | Shear strength of 90 MPa (1 mm welding) | Interfacial fracture | [24] |
| AZ31B (2 mm) | Q235 (1.2 mm) | Cu (100 μm) | Laser-TIG | Shear strength of 170 MPa (1 mm welding) | Interfacial fracture | [29] |
| AZ31B (2 mm) | Q235 (1.2 mm) | Ni (100 μm) | Laser-TIG | Shear strength of 166 MPa (1 mm welding) | Interfacial fracture | [29] |
| AZ31B (1 mm) | Q235A (1.5 mm) | Ni coating (20 μm) | Laser | 220 N/mm | Fusion zone | [7] |

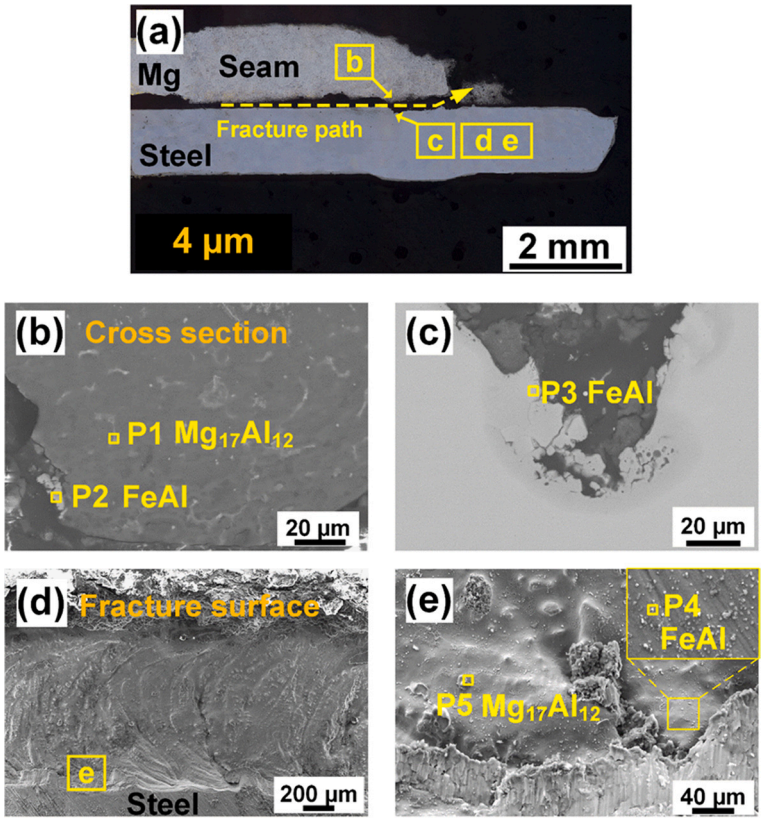


**Fig. 16.** Fracture analysis of magnesium/steel joint with Cu coating thickness of 4 μm: (a) fracture path of the joint; (b) weld side section analysis; (c) steel side section analysis; (d-e) fracture morphology analysis of steel side.

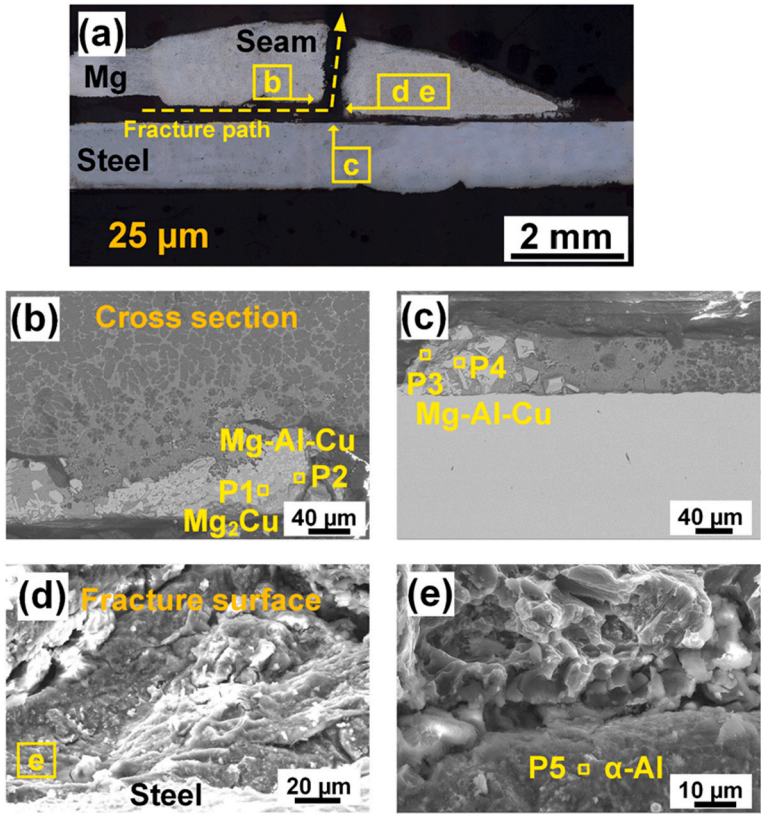


**Fig. 17.** Fracture analysis of magnesium/steel joint with Cu coating thickness of 25 μm: (a) fracture path of the joint; (b) weld side section analysis; (c) steel side section analysis; (d-e) fracture morphology analysis of steel side.

**Table 5**
EDS analysis of element content and possible phases of the points shown in the Fig. 16 (at. %).

| Point | Mg | Al | Fe | Cu | Possible phase |
|---|---|---|---|---|---|
| P1 | 73.21 | 25.23 | 0.52 | 1.05 | $Mg_{17}Al_{12}$ |
| P2 | 2.63 | 46.11 | 50.50 | 0.75 | FeAl |
| P3 | 0.14 | 32.27 | 66.97 | 0.61 | Fe+FeAl |
| P4 | 46.30 | 32.37 | 20.64 | 0.69 | ($\alpha$-Mg+FeAl) |
| P5 | 71.66 | 25.39 | 2.51 | 0.44 | $Mg_{17}Al_{12}$ |

**Table 6**
EDS analysis of element content and possible phases of the points shown in the Fig. 17 (at. %).

| Point | Mg | Al | Fe | Cu | Possible phase |
|---|---|---|---|---|---|
| P1 | 63.26 | 0.00 | 0.71 | 36.02 | $Mg_2Cu$ |
| P2 | 43.46 | 8.51 | 0.68 | 47.35 | Mg-Al-Cu Laves Phase |
| P3 | 43.95 | 13.91 | 1.56 | 40.58 | Mg-Al-Cu Laves Phase |
| P4 | 38.81 | 18.26 | 0.79 | 42.14 | Mg-Al-Cu Laves Phase |
| P5 | 2.95 | 95.32 | 1.39 | 0.33 | $\alpha$-Al |

Mg 46.30 at.%, Al 32.37 at.%, Fe 20.64 at.%) were also found at high magnification on the fracture surface. These results confirmed the role of FeAl reaction layer in Mg/steel joints: strengthening the interfacial metallurgical bonding and inhibiting crack propagation, thus improving the mechanical properties of Mg/steel joints.

Fig. 17 shows the fracture path and fracture morphology of the Mg/steel laser welding-brazing joint with 25 μm Cu coating thickness. The EDS energy spectrum analysis of the marked points is shown in Table 6. When coating thickness increased, the fracture path of the Mg/steel laser welding-brazing joint changed from interfacial fracture to seam fracture. According to previous SEM analysis of the joint, a large number of intermetallic compounds were generated at the interface of the intermediate region with increasing coating thickness. This process is often accompanied by cracks, which may have a negative impact on the performance of the joint. It can be clearly seen from SEM analysis of cross-sections on both sides of the fracture path (17 (b, c)), the fracture started from intermetallic compounds in the intermediate region, namely $Mg_2Cu$ eutectic structure (P1: Mg 63.26 at.%, Cu 36.02 at.%) and Mg-Al-Cu Laves phase (P2-P4). At the same time, the fracture surface morphology was a brittle fracture.

### 6.4. Interfacial reaction mechanism of Mg to Cu-coated steel

Thermocalc 2022a was used to simulate the cooling process in the FZ [56]. TCMG5 database was chosen to perform Scheil solidification simulations. The elemental content was set from the EDS of the FZ matrix (88.73 at.% Mg, 0.79 at.% Al, 0.48 at.% Fe, 10 at.% Cu). Due to the high cooling rate of the laser welding processing, the calculation assumes that solute diffuses instantly in the liquid and does not diffuse in the solid. The liquid/solid interface is thermodynamic equilibrium. Fig. 18 shows the temperature variation with the mole fraction of phases upon solidification. The diagram is helpful for analysing the metallurgical reactions during the welding-brazing process. Here, HTAL6MN5 and AL2FE represent FeAl phase, and CUMG2 represents the $Mg_2Cu$ phase. With cooling to full solidification, FeAl phase is generated first, then the C15 Laves phase and $Mg_2Cu$ phase.

Based on the observation of the interfacial microstructure and the thermodynamic analysis mentioned, a Mg/steel laser welding-brazing joint with Cu coating thickness of 11 μm at 1300 W power was selected to explain the interfacial connection mechanism.

In the heating stage, the AZ92 welding wire first melted and spread on the surface of Cu-coated steel and Cu coating melted under laser irradiation and heating, as shown in Fig. 19 (a). In the laser directly irradiated region, the laser impact force and the mixing of the molten

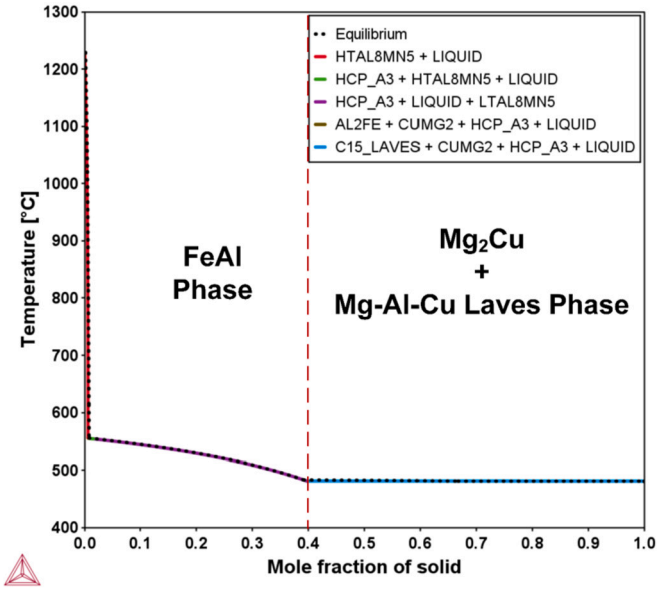


**Fig. 18.** Scheil solidification behaviour of fusion zone.

pool were strong. Thus, the Cu coating on the steel surface was completely melted and dissolved into the molten pool. Then as shown in Fig. 19 (b), elements in the molten pool began to diffuse: Al migrated from the molten pool to the steel substrate, while Cu diffused to the Mg-rich molten pool and aggregated at a certain distance from the steel surface. In the molten pool, Mg and Al paired up.

As the temperature dropped, between 1243 °C and 487 °C, the FeAl phase precipitated from the molten pool in the directly irradiated region, as shown in Fig. 19 (c). The Cu content in the intermediate region and the weld toe region was much more abundant. Cu atoms reacted with Mg atoms at 487 °C to form $\alpha$-Mg+$Mg_2Cu$ eutectic structure at the interface. These reaction layers would hinder the diffusion of Al atoms to the steel substrate, so it was difficult to generate the FeAl phase in the intermediate region and the weld toe region. At the same time, some Al atoms would replace Cu atoms in $Mg_2Cu$ and form massive Mg-Al-Cu Laves phases with different sizes within and around the $Mg_2Cu$ bulk. In the molten pool far away from the steel interface, Mg-Al atoms diffused with each other and eventually precipitated $Mg_{17}Al_{12}$. The final mircostructure distribution along the interface is shown in Fig. 19 (d).

## 7. Conclusions

This paper proposes a design framework mainly for the dissimilar joining of immiscible systems. It focuses on how to select the suitable metallic interlayer to control the interfacial reaction. The Miedema model has been developed to calculate the formation enthalpy and Gibbs free energy of formation for up to quaternary alloy systems. Combined with CALPHAD, the selection of intermediate layers was theoretically and systematically demonstrated.

This work chose AZ31B magnesium alloy to DP590 steel with a copper coating (Mg-Fe-Al-Cu quaternary system) as the object of analysis and prediction. The diffusion of each element and the formation of IMCs during the welding process are initially predicted. According to the prediction, Al atoms will diffuse from Mg FZ to the steel substrate and then form FeAl phase. Cu atoms will react with Mg and Al to form the Mg-Cu or Mg-Al-Cu LAVES phase.

This method can be applied to nearly all types of melt welding of dissimilar metals which are immiscible. The researchers can change the substrates, intermediate elements, and welding methods according to their demands. It would improve the efficiency and reliability of choosing suitable interlayers before experiments, which would help

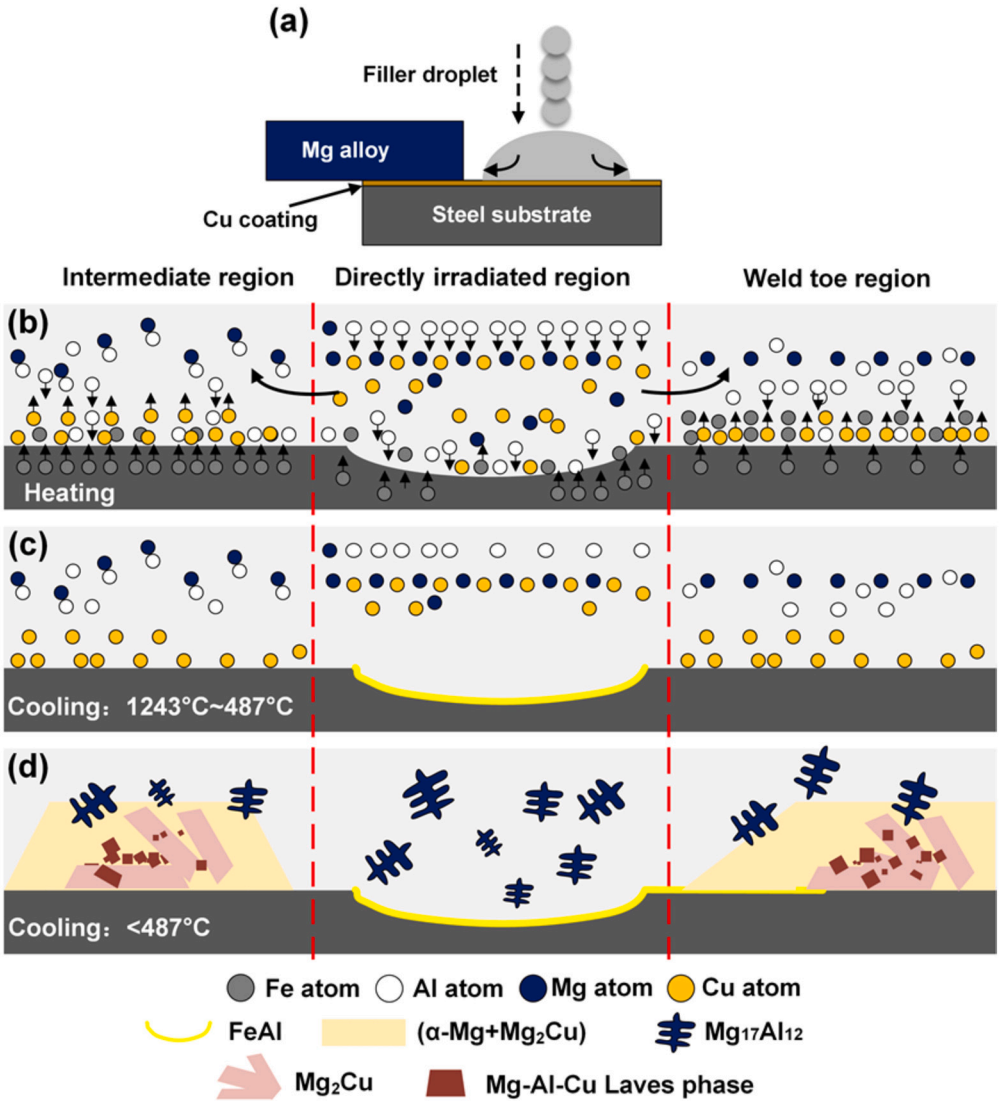


**Fig. 19.** Interfacial reaction mechanism of magnesium/copper-plated steel laser brazing-welding joint during welding-brazing process.

save the cost of time and resources. This framework mainly provides a theoretical prediction based on thermodynamics. In the future, if more numerical simulations of the welding process such as stress field simulation, deformation simulation, and heat source simulation are added to the framework, the prediction will be more accurate and will be an effective way to acquire favourable joints.

After the modelling, Cu coatings layers with different thicknesses (4 μm, 8 μm, 11 μm, 25 μm) were adopted to control the Mg/steel laser wire-filling welding-brazing joints. The effects of the presence of Cu coatings and the change of coating thickness on the weld development, interfacial morphology, microstructure and mechanical properties of the Mg/steel joints were compared. The effect of Cu on the intermetallic compounds was analysed, including the influence of Cu content on the types and quantities of intermetallic compounds. The change in mechanical properties was explained by the combination of interfacial microstructure, fracture path and fracture morphology. The main conclusions are:

(1) After adding Cu coating, the weld surface was well-formed without obvious defects and the weld section was stable. With an increase in Cu coating thickness, the weld width increased, indicating that the Cu coating was beneficial in improving the wetting and spreading of the filler wire on the steel surface.

(2) The microstructure of the Mg/steel brazing interface in three regions (intermediate, directly irradiated and weld toe regions) were different. A 5 μm Fe-Al reaction layer is always generated in the directly irradiated region. With Cu coating thickness increased, more Cu atoms were incorporated into the coral-shaped ($\alpha$-Mg+$Mg_2Cu$) eutectic, resulting in a transformation to massive $Mg_2Cu$ in the intermediate and weld toe region. Al atoms replaced part of Cu atoms in $Mg_2Cu$ and formed the Mg-Al-Cu Laves phase among it. But long cracks in the fusion zone are often generated within the thick eutectic structure.

(3) The thermodynamic calculation results indicate that Cu tended to aggregate above the steel substrate and attract Al, which diffused to the steel substrate and then formed the Fe-Al reaction layer in the directly irradiated region. The generation of the $Mg_2Cu$ and Mg-Al-Cu Laves phase was confirmed by Gibbs free energy calculations.

(4) The shear strength of Mg/steel joints reached a maximum at a 25 μm Cu coating thickness. The associated tensile-shear fracture load is 271 N/mm. The fracture modes are divided into two types: interfacial fracture and seam fracture. Interfacial fracture is attributed to inadequate metallurgical reaction along the Mg/steel interface. The increase in Cu promotes interfacial metallurgical reactions and the eutectic products are no longer network-like, but the overly thick hard and brittle phase reaction products tend to cause stress concentration and fracture at the joint from the fusion zone.

## CRediT authorship contribution statement

**Chengwei Zang:** Writing – original draft, Validation, Software, Methodology, Formal analysis, Conceptualization. **Xiaoye Zhao:** Methodology. **Hongbo Xia:** Software. **Wei Wen:** Writing – review & editing. **Zhuoming Tan:** Writing – review & editing, Formal analysis. **Caiwang Tan:** Supervision, Funding acquisition, Conceptualization. **Pedro E.J. Rivera-Díaz-del-Castillo:** Writing – review & editing, Supervision, Funding acquisition.

## Declaration of competing interest

The authors declare that they have no known competing financial interests or personal relationships that could have appeared to influence the work reported in this paper.

## Data availability

Data will be made available on request.

## Acknowledgements

The work was financially supported by National Natural Science Foundation of China (No. 51875129) and Natural Science Foundation for Excellent Young Scholars of Shandong Province (No. ZR2021YQ30). PEJRDC is grateful to the Engineering and Physical Sciences Research Council U.K. for the provision of funding via grant EP/L025213/1.

## Appendix A. Supplementary material

Supplementary material related to this article can be found online at https://doi.org/10.1016/j.matdes.2024.113050.

## References

[1] Gen Satoh, Y. Lawrence Yao, Caian Qiu, Strength and microstructure of laser fusion-welded ti–ss dissimilar material pair, Int. J. Adv. Manuf. Technol. 66 (2013) 469–479.
[2] Yanbin Chen, Shuhai Chen, Liqun Li, Influence of interfacial reaction layer morphologies on crack initiation and propagation in ti/al joint by laser welding–brazing, Mater. Des. 31 (1) (2010) 227–233.
[3] Min Zheng, Jin Yang, Jiayi Xu, Jiawei Jiang, Hua Zhang, Joao P. Oliveira, Xueqi Lv, Jing Xue, Zhuguo Li, Interfacial microstructure and strengthening mechanism of dissimilar laser al/steel joint via a porous high entropy alloy coating, J. Mater. Res. Technol. 23 (2023) 3997–4011.
[4] Fissha Biruke Teshome, Bei Peng, J.P. Oliveira, Jiajia Shen, Sansan Ao, Haoyue Li, Long Chen, Caiwang Tan, Xiaoguo Song, Naixun Zhou, et al., Role of pd interlayer on niti to ti6al4v laser welded joints: microstructural evolution and strengthening mechanisms, Mater. Des. 228 (2023) 111845.
[5] Hongbo Xia, Baiyun Yang, Jianhui Su, Yifan Liu, Xuan Su, Chong Wang, Xin Qiang, Tao Wu, Caiwang Tan, Improvement of laser welded tc4/cfrtp joint strength by combination of surface modification of Mao and laser texturing, Thin-Walled Struct. 196 (2024) 111409.
[6] Rui Cao, J.H. Chang, Qian Huang, X.B. Zhang, Y.J. Yan, J.H. Chen, Behaviors and effects of zn coating on welding-brazing process of al-steel and mg-steel dissimilar metals, J. Manuf. Process. 31 (2018) 674–688.
[7] Xiaoye Zhao, Caiwang Tan, Liyuan Xiao, Hongbo Xia, Bo Chen, Xiaoguo Song, Liqun Li, Jicai Feng, Effect of the ni coating thickness on laser welding-brazing of mg/steel, J. Alloys Compd. 769 (2018) 1042–1058.
[8] Caiwang Tan, Liqun Li, Yanbin Chen, Wei Guo, Laser-tungsten inert gas hybrid welding of dissimilar metals az31b mg alloys to zn coated steel, Mater. Des. 49 (2013) 766–773.
[9] Caiwang Tan, Jia Yang, Xiaoye Zhao, Kaiping Zhang, Xiaoguo Song, Bo Chen, Liqun Li, Jicai Feng, Influence of ni coating on interfacial reactions and mechanical properties in laser welding-brazing of mg/ti butt joint, J. Alloys Compd. 764 (2018) 186–201.
[10] Qinghua Li, Zhongwei Ma, Shude Ji, Qi Song, Peng Gong, Rui Li, Effective joining of mg/ti dissimilar alloys by friction stir lap welding, J. Mater. Process. Technol. 278 (2020) 116483.
[11] Chengwei Zang, Jinge Liu, Caiwang Tan, Kaiping Zhang, Xiaoguo Song, Bo Chen, Liqun Li, Jicai Feng, Laser conduction welding characteristics of dissimilar metals mg/ti with al interlayer, J. Manuf. Process. 32 (2018) 595–605.
[12] Caiwang Tan, Chengwei Zang, Hongbo Xia, Xiaoye Zhao, Kaiping Zhang, Shenghao Meng, Bo Chen, Xiaoguo Song, Liqun Li, Influence of al additions in zn–based filler metals on laser welding–brazing of al/steel, J. Manuf. Process. 34 (2018) 251–263.
[13] Hongbo Xia, Baiyun Yang, Yongdian Han, Lianyong Xu, Caiwang Tan, Liqun Li, Haoyue Li, Xiaoye Zhao, Kaiping Zhang, Xuan Su, et al., Toward understanding the fractured mechanism in laser welded–brazed al/steel interface by in–situ sem tensile observations, J. Mater. Process. Technol. 325 (2024) 118294.
[14] D.M. Fronczek, J. Wojewoda-Budka, R. Chulist, A. Sypien, A. Korneva, Z. Szulc, N. Schell, P. Zieba, Structural properties of ti/al clads manufactured by explosive welding and annealing, Mater. Des. 91 (2016) 80–89.
[15] V.R. Ryabov, D.M. Rabkin, L.G. Strizhevskaya, Welding of Dissimilar Metals, 2003.
[16] Sergey Kuryntsev, A review: laser welding of dissimilar materials (al/fe, al/ti, al/cu)—methods and techniques, microstructure and properties, Materials 15 (1) (2021) 122.
[17] Yongjian Fang, Xiaosong Jiang, Defeng Mo, Degui Zhu, Zhiping Luo, A review on dissimilar metals' welding methods and mechanisms with interlayer, Int. J. Adv. Manuf. Technol. 102 (2019) 2845–2863.
[18] Liming Liu, Xiaodong Qi, Zhonghui Wu, Microstructural characteristics of lap joint between magnesium alloy and mild steel with and without the addition of sn element, Mater. Lett. 64 (1) (2010) 89–92.
[19] Liqun Li, Caiwang Tan, Yanbin Chen, Wei Guo, Xinbin Hu, Influence of zn coating on interfacial reactions and mechanical properties during laser welding-brazing of mg to steel, Metall. Mater. Trans. A 43 (2012) 4740–4754.
[20] Liqun Li, Caiwang Tan, Yanbin Chen, Wei Guo, Changxing Mei, Co2 laser welding–brazing characteristics of dissimilar metals az31b mg alloy to zn coated dual phase steel with mg based filler, J. Mater. Process. Technol. 213 (3) (2013) 361–375.
[21] Caiwang Tan, Liyuan Xiao, Fuyun Liu, Bo Chen, Xiaoguo Song, Liqun Li, Jicai Feng, Influence of laser power on the microstructure and mechanical properties of a laser welded-brazed mg alloy/ni-coated steel dissimilar joint, J. Mater. Eng. Perform. 26 (2017) 2983–2997.
[22] Waled M. Elthalabawy, Tahir I. Khan, Microstructural development of diffusion-brazed austenitic stainless steel to magnesium alloy using a nickel interlayer, Mater. Charact. 61 (7) (2010) 703–712.
[23] Waled Elthalabawy, Tahir Khan, Liquid phase bonding of 316l stainless steel to az31 magnesium alloy, J. Mater. Sci. Technol. 27 (1) (2011) 22–28.
[24] Xiaodong Qi, Gang Song, Interfacial structure of the joints between magnesium alloy and mild steel with nickel as interlayer by hybrid laser-tig welding, Mater. Des. 31 (1) (2010) 605–609.
[25] Waled M. Elthalabawy, Tahir I. Khan, Eutectic bonding of austenitic stainless steel 316l to magnesium alloy az31 using copper interlayer, Int. J. Adv. Manuf. Technol. 55 (2011) 235–241.
[26] Daxin Ren, Liming Liu, Interface microstructure and mechanical properties of arc spot welding mg–steel dissimilar joint with cu interlayer, Mater. Des. 59 (2014) 369–376.
[27] X.Y. Wang, D.Q. Sun, Y. Sun, Influence of cu-interlayer thickness on microstructures and mechanical properties of mig-welded mg-steel joints, J. Mater. Eng. Perform. 25 (2016) 910–920.
[28] Liming Liu, Xiaodong Qi, Effects of copper addition on microstructure and strength of the hybrid laser-tig welded joints between magnesium alloy and mild steel, J. Mater. Sci. 44 (2009) 5725–5731.
[29] Liming Liu, Xiaodong Qi, Strengthening effect of nickel and copper interlayers on hybrid laser-tig welded joints between magnesium alloy and mild steel, Mater. Des. 31 (8) (2010) 3960–3963.
[30] Taotao Li, Gang Song, Peini Yu, Liming Liu, Interfacial microstructure evolution in fusion welding of immiscible mg/fe system, Mater. Des. 181 (2019) 107903.
[31] Caiwang Tan, Xiaoguo Song, Bo Chen, Liqun Li, Jicai Feng, Enhanced interfacial reaction and mechanical properties of laser welded-brazed mg/ti joints with al element from filler, Mater. Lett. 167 (2016) 38–42.
[32] Zequn Zhang, Caiwang Tan, Xiaoye Zhao, Bo Chen, Xiaoguo Song, Hongyun Zhao, Influence of cu coating thickness on interfacial reactions in laser welding-brazing of mg to ti, J. Mater. Process. Technol. 261 (2018) 61–73.
[33] Tao Yang, Wei Dai, Long Chen, Yuan Zhuang, Zengming Zhou, Juncheng Hu, Thermodynamically revealing the effect mechanism of cu on the interfacial metallurgical reaction for al/steel welding-brazing joint, J. Mater. Process. Technol. 299 (2022) 117372.
[34] Jinge Liu, Caiwang Tan, Laijun Wu, Xiaoye Zhao, Zequn Zhang, Bo Chen, Xiaoguo Song, Jicai Feng, Butt laser welding-brazing of az31mg alloy to cu coated ti-6al-4v with az92 mg based filler, Opt. Laser Technol. 117 (2019) 200–214.
[35] S. Asadi, T. Saeid, A. Valanezhad, I. Watanabe, J. Khalil-Allafi, Effects of ni powder addition on microstructure and mechanical properties of niti to aisi 304 stainless steel archwire dissimilar laser welds, J. Manuf. Process. 55 (2020) 13–21.
[36] Saeed Asadi, Tohid Saeid, Farzad Habibi, Yejin Kim, Alireza Valanezhad, Nokeun Park, Phase identification and thermodynamic modeling of a quaternary system in dissimilar laser-welded niti/ass, J. Mater. Res. Technol. 16 (2022) 25–38.
[37] Jiajia Shen, Rita Gonçalves, Yeon Taek Choi, J.G. Lopes, Jin Yang, N. Schell, Hyoung Seop Kim, J.P. Oliveira, Microstructure and mechanical properties of gas metal arc welded cocrfemnni joints using a 308 stainless steel filler metal, Scr. Mater. 222 (2023) 115053.
[38] Joao Pedro Oliveira, Jiajia Shen, Z. Zeng, Jeong Min Park, Yeon Taek Choi, N. Schell, E. Maawad, N. Zhou, Hyoung Seop Kim, Dissimilar laser welding of a cocrfemnni high entropy alloy to 316 stainless steel, Scr. Mater. 206 (2022) 114219.

[39] Luke Walker, Carolin Fink, Colleen Hilla, Ying Lu, Wei Zhang, Peculiar roles of nickel diffusion in intermetallic compound formation at the dissimilar metal interface of magnesium to steel spot welds, Mater. Des. 230 (2023) 111980.
[40] C. Aguilar, P. Guzman, S. Lascano, C. Parra, L. Bejar, A. Medina, D. Guzman, Solid solution and amorphous phase in ti–nb–ta–mn systems synthesized by mechanical alloying, J. Alloys Compd. 670 (2016) 346–355.
[41] W.C. Wang, J.H. Li, H.F. Yan, B.X. Liu, A thermodynamic model proposed for calculating the standard formation enthalpies of ternary alloy systems, Scr. Mater. 56 (11) (2007) 975–978.
[42] M. Rafiei, M.H. Enayati, F. Karimzadeh, Thermodynamic analysis of solid solution formation in the nanocrystalline fe–ti–al ternary system during mechanical alloying, J. Chem. Thermodyn. 59 (2013) 243–249.
[43] J.F. Herbst, On estimating the enthalpy of formation and hydrogen content of quaternary hydrides, J. Alloys Compd. 368 (1–2) (2004) 221–228.
[44] Kuo-Chih Chou, A general solution model for predicting ternary thermodynamic properties, Calphad 19 (3) (1995) 315–325.
[45] E. Bonnier, R. Caboz, Sur lestimation de lenthalpie libre de melange de certains alliages metalliques liquides ternaires, C. R. Hebd. Séances Acad. Sci. 250 (3) (1960) 527–529.
[46] Yves M. Muggianu, Michele Gambino, J.P. Bros, Enthalpies of formation of liquid alloys bismuth-gallium-tin at 723k-choice of an analytical representation of integral and partial thermodynamic functions of mixing for this ternary-system, J. Chim. Phys. 72 (1) (1975) 83–88.
[47] Ninshu Ma, Liqun Li, Hui Huang, Shuai Chang, Hidekazu Murakawa, Residual stresses in laser-arc hybrid welded butt-joint with different energy ratios, J. Mater. Process. Technol. 220 (2015) 36–45.
[48] He Yang, Liang Huang, Mei Zhan, Coupled thermo-mechanical fe simulation of the hot splitting spinning process of magnesium alloy az31, Comput. Mater. Sci. 47 (3) (2010) 857–866.
[49] S.T. Auwal, Singh Ramesh, Zequn Zhang, Jinge Liu, Caiwang Tan, Sunusi Marwana Manladan, Farazila Yusof, Faris Tarlochan, Influence of electrodeposited cu-ni layer on interfacial reaction and mechanical properties of laser welded-brazed mg/ti lap joints, J. Manuf. Process. 37 (2019) 251–265.
[50] A. Bachmaier, M. Kerber, D. Setman, R. Pippan, The formation of supersaturated solid solutions in fe–cu alloys deformed by high-pressure torsion, Acta Mater. 60 (3) (2012) 860–871.
[51] Ming Xiao, Chenkai Gao, Caiwang Tan, Yixuan Zhao, Hongbing Liu, Jin Yang, Experimental and numerical assessment of interfacial microstructure evolution in dissimilar al/steel joint by diode laser welding-brazing, Optik 245 (2021) 167706.
[52] Holger Laukant, Clemens Wallmann, Markus Müller, M. Korte, B. Stirn, H-G. Haldenwanger, U. Glatzel, Fluxless laser beam joining of aluminium with zinc coated steel, Sci. Technol. Weld. Join. 10 (2) (2005) 219–226.
[53] Tianhao Wang, Piyush Upadhyay, Scott Whalen, A review of technologies for welding magnesium alloys to steels, Int. J. Precis. Eng. Manuf.-Green Technol. 8 (2021) 1027–1042.
[54] L.M. Liu, Xu Zhao, Study on the weld joint of mg alloy and steel by laser-gta hybrid welding, Mater. Charact. 59 (9) (2008) 1279–1284.
[55] M. Wahba, S. Katayama, Laser welding of az31b magnesium alloy to zn-coated steel, Mater. Des. 35 (2012) 701–706.
[56] Jan-Olof Andersson, Thomas Helander, Lars Höglund, Pingfang Shi, Bo Sundman, Thermo-calc & dictra, computational tools for materials science, Calphad 26 (2) (2002) 273–312.